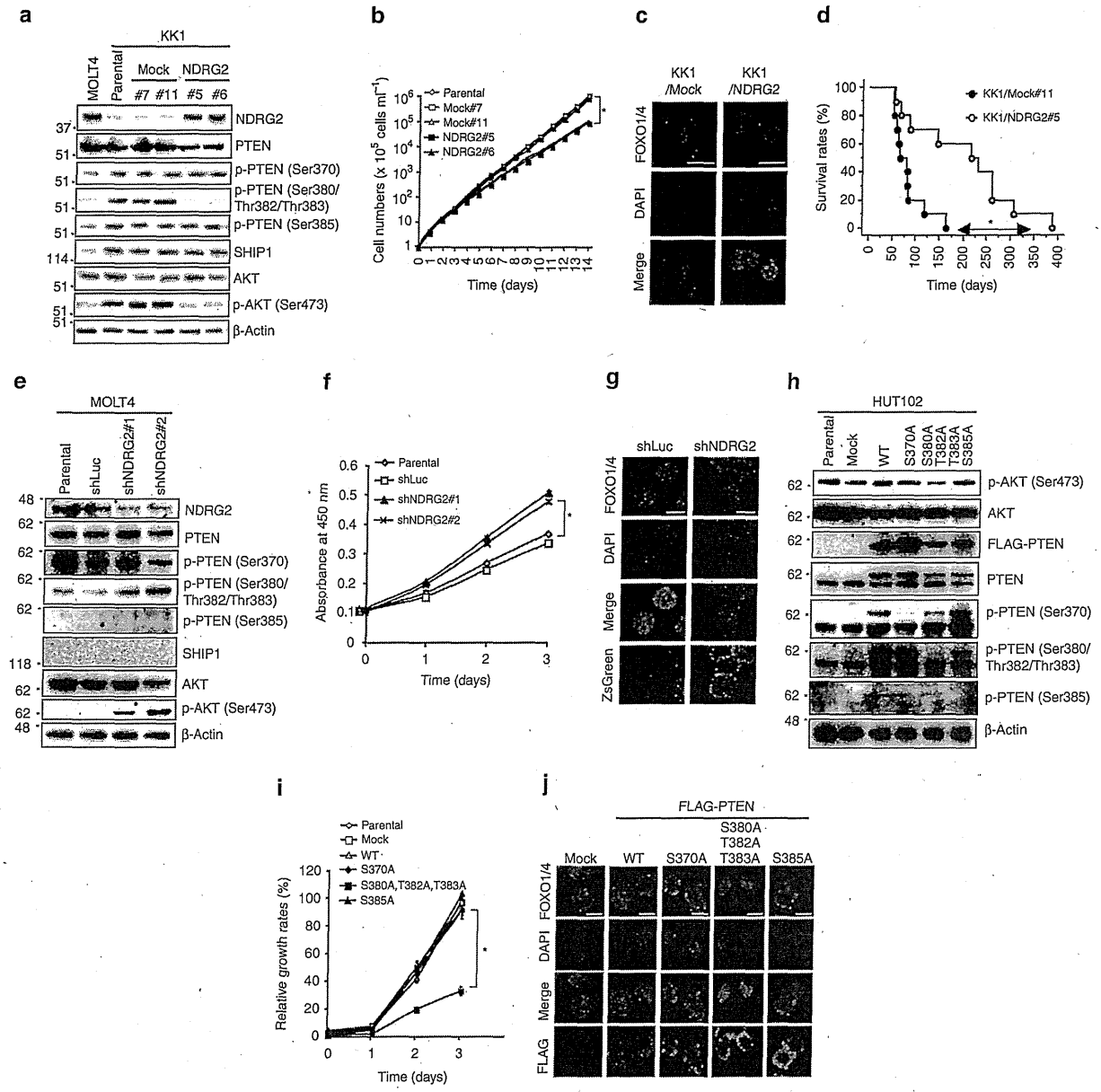

Figure 3 | Decreased expression of *NDRG2* and the enhanced phosphorylation of PTEN are involved in the activation of PI3K-AKT. (**a**) Western blots analysis of stably transfected KK1 cells. Note that the amount of NDRG2 protein in both MOLT4 and NDRG2-transfected KK1 cells was found to be similar. The data are representative of three experiments. (**b**) The proliferation rates of KK1-NDRG2, KK1-Mock, and parental KK1 cells. The mean ± s.d. is shown; $*P<0.05$ (Student's *t*-test). The data are representative of three experiments. (**c**) The subcellular localization of FOXO1/4 in KK1-NDRG2 and KK1-Mock cells. The nuclei were labelled with DAPI. Scale bar, 10 μm. The data are representative of three experiments. (**d**) Kaplan–Meier survival curves of NOG mice intravenously injected with KK1-NDRG2 or KK1-Mock cells ($n=10$ mice per group, $*P<0.05$, log-rank test). (**e**) MOLT4 cells transiently transfected with two different shRNAs against NDRG2 or control shRNA against luciferase (shLuc) were subjected to western blotting. The data are representative of three experiments. (**f**) The proliferation rates of MOLT4 cells transfected with shNDRG2 or shLuc expression vectors. The mean ± s.d. is shown; $*P<0.05$ (Student's *t*-test). The data are representative of three experiments. (**g**) The subcellular localization of FOXO1/4 in MOLT4 cells transfected with shNDRG2 or shLuc. The transfected cells were visualized by ZsGreen expression. Scale bar, 10 μm. The data are representative of three experiments. (**h**) HUT102 cells transfected with WT PTEN or PTEN mutants were subjected to western blotting. A slower migrating band for PTEN and phosphorylated PTEN appears in the presence of transfected PTEN, and a high level of phosphorylation of exogenous PTEN-Ser380/Thr382/Thr383 was observed in HUT102 cells. The data are representative of three experiments. (**i**) The proliferation rates of HUT102 cells transfected with WT or mutant PTEN. The mean ± s.d. is shown; $*P<0.05$ (Student's *t*-test). The data are representative of three experiments. (**j**) The subcellular localization of FOXO1/4 in HUT102 cells transfected with WT or mutant PTEN. The transfected cells were visualized using an antibody against FLAG. Scale bar, 10 μm. The data are representative of three experiments.

Thr383 cluster in the presence or absence of increasing concentrations of okadaic acid (OA), an inhibitor of the serine–threonine phosphatases, PP1 and PP2A[28]. We incubated KK1/NDRG2 cell lysates with the synthetic pSer380/pThr382/pThr383 peptide in the presence or absence of increasing concentrations of OA. As expected, the phosphatase activity in

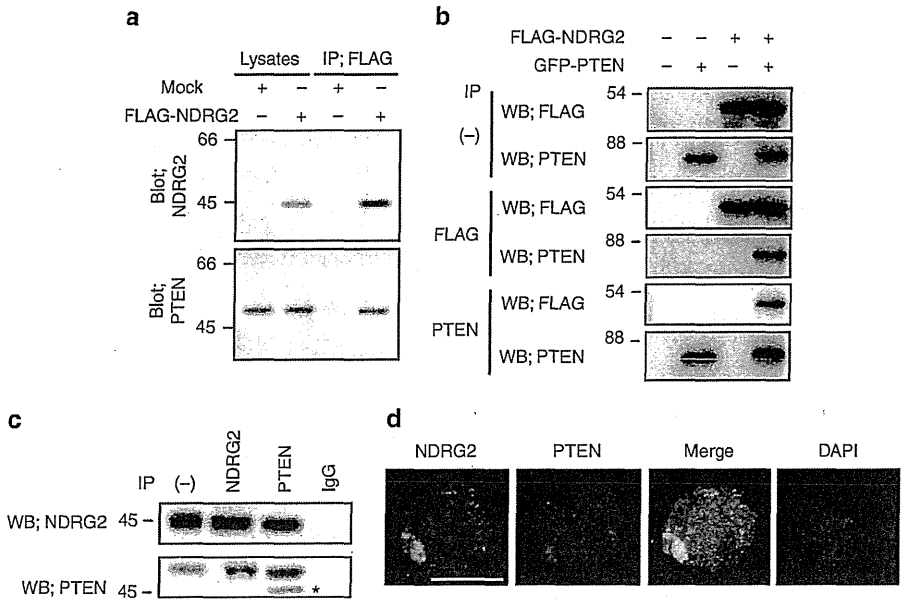

Figure 4 | NDRG2 is a novel PTEN-interacting protein. (**a**) The KK1 cell lysates transfected with the mock or FLAG-NDRG2 vector were immunoprecipitated with an anti-FLAG antibody, and the western blots were probed with the indicated antibodies. IP, immunoprecipitation. The data are representative of three experiments. (**b**) Exogenously expressed PTEN and NDRG2 were co-immunoprecipitated in 293T cells (WB, western blot). The data are representative of three experiments. (**c**) The co-immunoprecipitation of endogenous PTEN and NDRG2 was performed in MOLT4 cell lysates. On the input lane (–), 1/200 of the input was loaded for detection of NDRG2. Asterisk, nonspecific band. The data are representative of three experiments. (**d**) The co-localization of endogenous PTEN and NDRG2 was determined in MOLT4 cells. The nuclei were labelled with DAPI. Scale bar, 10 μm. The data are representative of three experiments.

KK1-NDRG2 cell lysates was substantially inhibited by a low concentration of OA (10 nM) (Fig. 5a). In addition, the dephosphorylation of PTEN-Ser380/Thr382/Thr383 in KK1-NDRG2 cells was inhibited by OA in a dose-dependent manner (Fig. 5b), but there was no effect on PTEN-Ser370 phosphorylation. In accordance with these results, a transiently expressed PP2A catalytic subunit (PP2Ac), but not PP1c or PP5c, efficiently dephosphorylated the synthetic pSer380/pThr382/pThr383 peptide, which was prevented by 10 nM OA (Fig. 5c; Supplementary Fig. 16). Similarly, the endogenous PP2Ac immunoprecipitated from NIH3T3 lysates exhibited phosphatase activity toward the pSer380/pThr382/pThr383 peptide in an OA-sensitive manner (Fig. 5d; Supplementary Fig. 17). In support of these data, small interfering RNA (siRNA)-mediated knockdown of PP2Acα prevented the NDRG2-dependent PTEN dephosphorylation in KK1-NDRG2 cells (Supplementary Fig. 18). Further analysis revealed that the recombinant PP2A core enzyme, a dimer of PP2Ac and the structural A subunit, also dephosphorylated the pSer380/pThr382/pThr383 peptide and was capable of dephosphorylating each of the three phosphorylated residues (pSer380, pThr382 and pThr383) with comparable efficiencies (Fig. 5e). Recombinant PP2A dephosphorylated PTEN-Ser380/Thr382/Thr383 purified from KK1 cell lysates (Fig. 5f), indicating that PP2A specifically mediates the dephosphorylation of PTEN-Ser380/Thr382/Thr383. We demonstrated that PP2Ac co-precipitated with NDRG2 in the lysates of crosslinked HUT102/NDRG2 cells (Fig. 5g). Although PP2Ac was barely detectable in the PTEN immunoprecipitates from KK1-Mock cells (Fig. 5h), PTEN clearly co-precipitated with both NDRG2 and PP2Ac in KK1-NDRG2 cells; this result was accompanied by decreased PTEN-Ser380/Thr382/Thr383 phosphorylation (Fig. 5h), suggesting that NDRG2 recruits PP2A to PTEN and thereby promotes PTEN-Ser380/Thr382/Thr383 dephosphorylation. Remarkably, we found that C-terminal deletion mutants of NDRG2 (ΔC and NDR), which do not interact with PP2A, are impaired in their ability to downregulate PTEN-Ser380/Thr382/Thr383 phosphorylation (Supplementary Fig. 19).

***NDRG2*-deficient mice are susceptible to spontaneous tumours.** To determine whether NDRG2 has a role in tumourigenesis, we generated *NDRG2*-deficient (*NDRG2*$^{-/-}$) mice (Supplementary Fig. 20), which were born at normal Mendelian ratios (Supplementary Table 5) and developed without apparent physical abnormalities. NDRG2 was highly expressed in the adult mouse brain, heart and liver[29] (Fig. 6a). The mutant mice exhibited increased levels of phosphorylated PTEN-Ser380/Thr382/Thr383, AKT-Ser473 and GSK3β-Ser9 in all of the tissues examined (Fig. 6b). In addition to the NDRG2 and PTEN interaction in the frontal cortex of wild-type (WT) mice (Fig. 6c), the *NDRG2*$^{-/-}$ embryonic fibroblasts exhibited increased phosphorylated PTEN-Ser380/Thr382/Thr383, high AKT-Ser473 phosphorylation and an accelerated cell proliferation rate (Fig. 6d,e). The *NDRG2*$^{-/-}$ mice had a markedly shorter lifespan than the WT or *NDRG2*$^{+/-}$ mice (Fig. 6f), and they developed various types of tumours, including lymphoma, hepatocellular carcinoma and bronchoalveolar carcinoma (Supplementary Table 6; Fig. 6g,h). Malignant lymphomas occurred at a high frequency (~50%), and the infiltrating lymphoid cells were $CD3^+CD4^+CD8^-$, indicating a mature helper T-cell phenotype (Fig. 6i–n; Supplementary Fig. 21), suggesting that NDRG2 is a possible tumour suppressor in various types of cancer, including peripheral T-cell lymphoma.

***NDRG2* downregulation activates PI3K-AKT in various cancers.** We next evaluated the methylation status of the *NDRG2* promoter in various cancer cell lines from different organ origins.

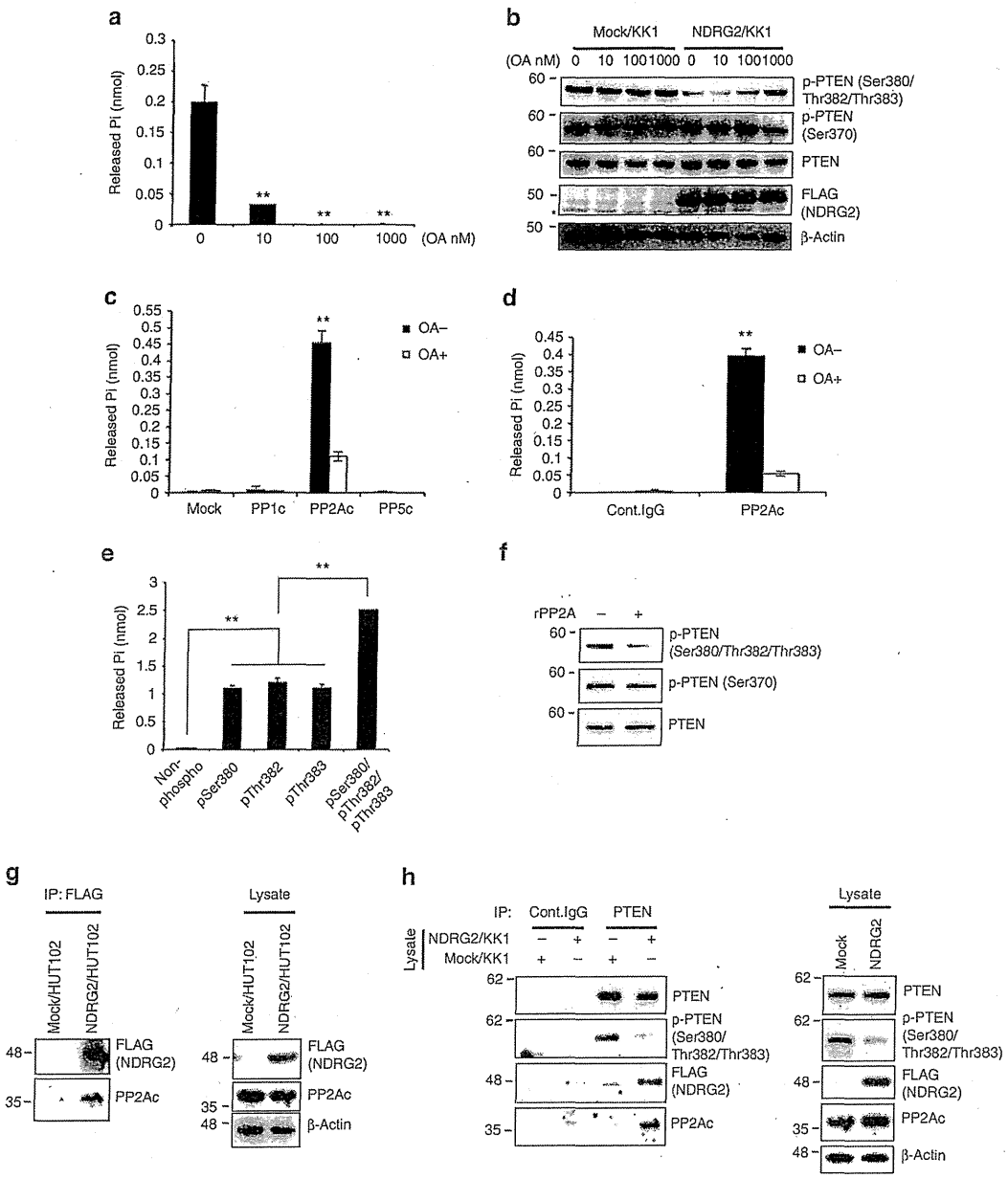

Figure 5 | NDRG2 recruits PP2A to PTEN leading to its dephosphorylation at pSer380/pThr382/pThr383. (**a**) KK1-NDRG2 cell lysates were incubated with a pSer380/pThr382/pThr383 PTEN phosphopeptide in the presence or absence of different concentrations of OA. The amount of released phosphate was quantitated using the malachite green assay. The mean ± s.d. is shown; $^{**}P<0.05$ compared with untreated control (Student's *t*-test). The data are representative of three experiments. (**b**) KK1-Mock and KK1-NDRG2 cells were treated with increasing concentrations of OA for 2 h and subjected to western blot analysis. Asterisk, nonspecific band. The data are representative of three experiments. (**c**) After immunoprecipitating lysates from 293T cells transfected with the indicated vectors, the beads were incubated with a pSer380/pThr382/pThr383 phosphopeptide in the presence or absence of 10 nM OA, and phosphate release was determined. The mean ± s.d. is shown; $^{**}P<0.05$ (Student's *t*-test). The data are representative of three experiments. (**d**) After immunoprecipitating the NIH3T3 lysates with an anti-PP2Ac antibody, the beads were incubated with a pSer380/pThr382/pThr383 phosphopeptide in the presence or absence of 10 nM OA, and phosphate release was determined. The mean ± s.d. is shown; $^{**}P<0.05$ (Student's *t*-test). The data are representative of three experiments. (**e**) 0.5 unit of recombinant PP2A was incubated with 200 μg ml^{-1} of either PTEN peptide or the phosphopeptides containing either pSer380, pThr382, pThr383 or pSer380/pThr382/pThr383, and phosphate release was determined. The mean ± s.d. is shown; $^{**}P<0.05$ (Student's *t*-test). The data are representative of three experiments. (**f**) The beads were incubated with or without recombinant PP2A after immunoprecipitating the KK1-Mock lysates with an anti-PTEN antibody. Western blot analysis of the reaction mixtures was performed to determine the degree of phosphorylation of PTEN. The data are representative of two experiments. (**g**) The lysates of HUT102-NDRG2 or HUT102-Mock cells treated with the crosslinker DTBP were immunoprecipitated with an anti-FLAG antibody and subsequently probed for co-precipitated PP2Ac by Western blotting. The data are representative of three experiments. (**h**) The lysates from KK1-NDRG2 or KK1-Mock cells treated with DTBP were immunoprecipitated with an anti-PTEN antibody, and the Western blots were probed with the indicated antibodies. Asterisk, nonspecific band. The data are representative of three experiments.

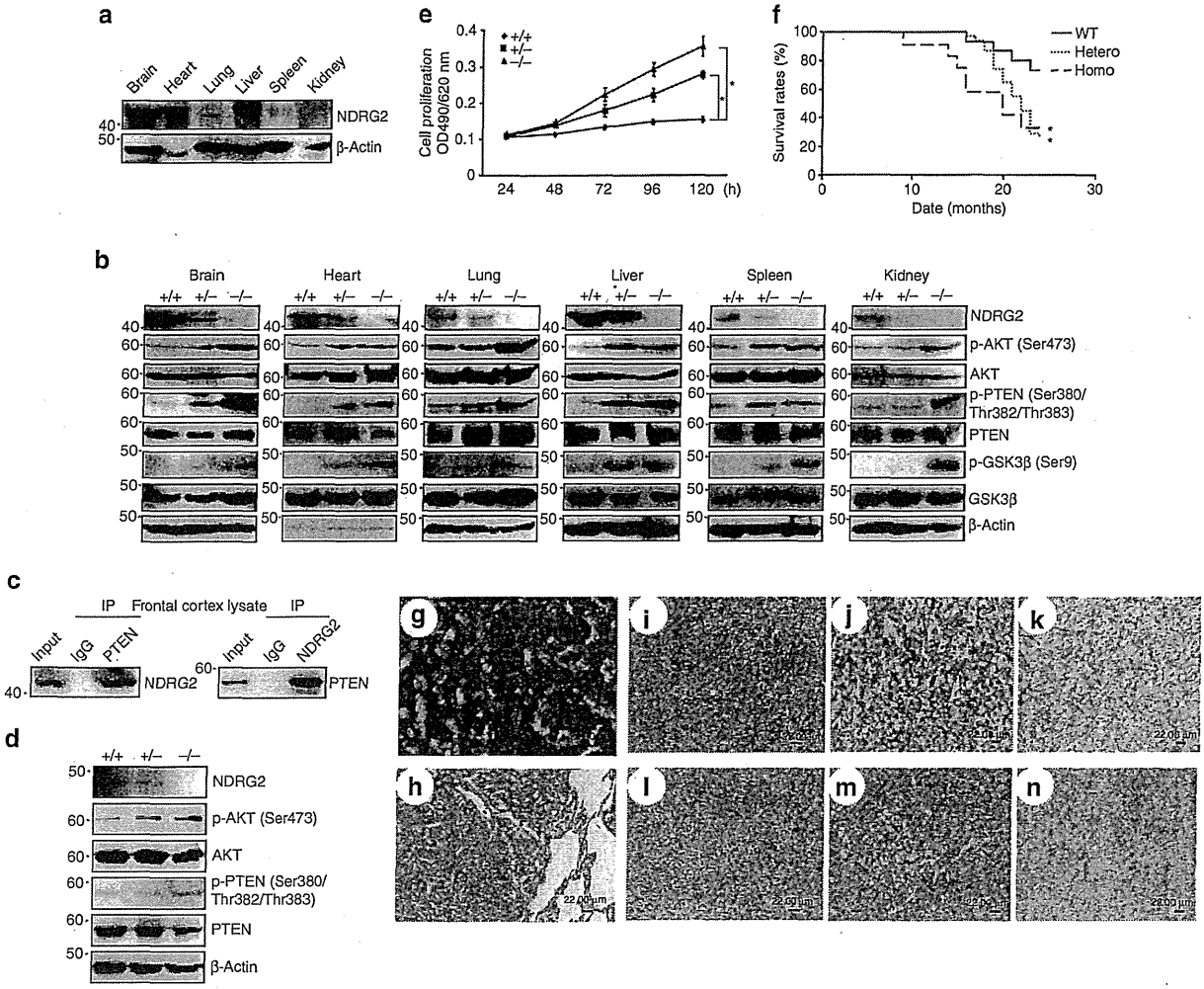

Figure 6 | *NDRG2*-deficient mice are susceptible to tumour formation. (**a**) Western blots of 3-month-old adult tissues of WT mice. The data are representative of two experiments. (**b**) Western blots of various tissues of 3-month-old *NDRG2*-deficient mice. The data are representative of two experiments. (**c**) The co-immunoprecipitation of PTEN and NDRG2 in frontal cortex homogenates from 3-month-old WT mice. The data are representative of three experiments. (**d**) Whole-cell lysates from WT, $NDRG2^{+/-}$ and $NDRG2^{-/-}$ embryonic fibroblasts were subjected to western blotting. (**e**) The proliferation rates of WT, $NDRG2^{+/-}$, and $NDRG2^{-/-}$ embryonic fibroblasts. The mean ± s.d. is shown; $^{*}P<0.05$ (Student's *t*-test). The data are representative of three experiments. (**f**) Kaplan–Meier survival curves of WT ($n=15$), $NDRG2^{+/-}$ ($n=31$) and $NDRG2^{-/-}$ ($n=12$) mice up to 24 months of age. The difference in survival was statistically significant between WT and $NDRG2^{+/-}$ or $NDRG2^{-/-}$ mice ($^{*}P<0.05$, log-rank test). (**g**) A hepatocellular carcinoma section from an $NDRG2^{+/-}$ mouse liver was subjected to H&E staining. The results indicated the presence of a large sheet of hepatic cords composed of several hepatocytes of variable nuclei and cell sizes; the nuclei of the carcinoma cells were hyperchromatic with prominent nucleoli (scale bar, 22 μm). (**h**) A bronchoalveolar carcinoma section from an $NDRG2^{+/-}$ mouse lung was subjected to H&E staining. The histopathology demonstrated a well-circumscribed mass of a solid sheet of neoplastic cells containing hyperchromatic nuclei with signs of frequent mitosis and an indistinct basophilic cytoplasm (scale bar, 22 μm). (**i–k**) Lymphoma sections from the mesenteric lymph node of an $NDRG2^{+/-}$ mouse. The histopathology indicated the presence of diffuse pleomorphic large lymphoid cells with vesicular nuclei, prominent nucleoli and scant cytoplasm (**i**). Robust staining for CD3 was present in the cytoplasm (**j**), but B220 staining was negative (**k**) (scale bar, 22 μm). (**l–n**) Lymphoma sections from an $NDRG2^{+/-}$ mouse spleen were examined by histopathology. The results demonstrated pleomorphic large lymphoid cells with vesicular nuclei, prominent nucleoli, some nuclear distortion and numerous cells undergoing mitosis (**l**). Staining for CD3 revealed robust cytoplasmic staining in cells, ranging from white pulp to red pulp (**m**). B220 staining was negative (**n**) (scale bar, 22 μm).

In accordance with previous studies[30,31], methylation of the *NDRG2* promoter was found in various cancer types (Supplementary Table 7; Fig. 7a). We confirmed that treatment of these cancer cell lines with 5-aza-deoxycytidine resulted in an increased abundance of *NDRG2* mRNA (Fig. 7b). Recently, we reported that the abundance of phosphorylated AKT-Ser473 inversely correlated well with NDRG2 protein abundance in the majority of oral squamous cell carcinoma (OSCC) cases[32], which are known to have very low frequencies of *PTEN* and *PIK3CA* mutations[33,34]. We found that cancer cell lines with low levels of NDRG2 show high levels of phosphorylated PTEN-Ser380/Thr382/Thr383 and AKT-Ser473 (Fig. 7c). Of note, we found that the ectopic expression of NDRG2 in two human cancer cell lines carrying WT *PTEN* ((SAS (OSCC) and HeLa (cervical cancer)) resulted in marked decreases in PTEN-Ser380/Thr382/Thr383 phosphorylation and PI3K-AKT inactivation (Fig. 7d). These findings suggest that down-regulation of *NDRG2* could have an important role in activating the PI3K-AKT signalling pathway in various types of cancer.

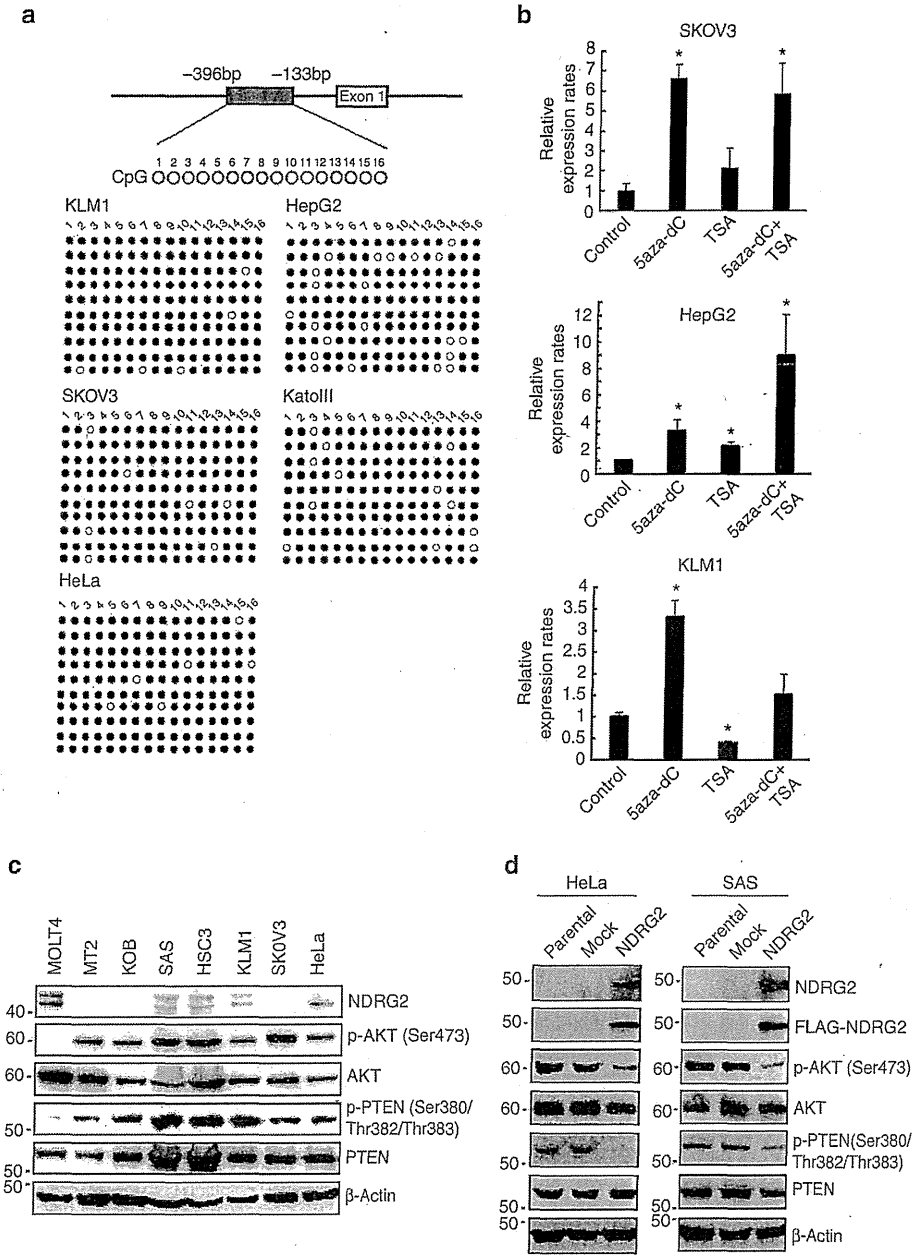

Figure 7 | Downregulation of *NDRG2* is associated with enhanced phosphorylation of PTEN-Ser380/Thr382/Thr383 and enhanced activation of PI3K-AKT in various cancers. (**a**) Bisulfite genomic sequencing of the *NDRG2* promoter region in the KLM1 (pancreatic cancer), SKOV3 (ovarian cancer), HeLa (cervical cancer), HepG2 (hepatic cancer) and KatoIII (gastric cancer) cell lines. PCR products amplified from bisulfite-treated genomic DNA were subcloned, and ten clones in each cell line were sequenced. Open circles indicate unmethylated CpGs (Thy) and filled circles indicate methylated CpGs (Cyt). The region sequenced spans from −396 bp to −133 bp. (**b**) SKOV3, HepG2 and KLM1 cells were cultured with 10 μM 5-aza-dC for 72 h, with 1.2 μM TSA for 48 h, or with 1.2 μM of TSA for 48 h, followed by 10 μM of 5-aza-dC for 24 h. After treatments, total RNA was extracted and quantitative RT-PCR was performed with *NDRG2* and β-actin. The relative amounts of mRNA were normalized against β-actin mRNA and expressed relative to the mRNA abundance in untreated cells. The mean ± s.d. is shown; $^*P<0.05$ compared with the untreated control (Student's *t*-test). The data are representative of two experiments. (**c**) Western blot analyses of NDRG2, PTEN, p-PTEN (Ser380/Thr382/Thr383), AKT and p-AKT (Ser473) were performed in SAS (OSCC), HSC3 (OSCC), KLM1, SKOV3, HeLa, MT2 (ATLL), KOB (ATLL) and MOLT4 (T-ALL) cell lines. The data are representative of two experiments. (**d**) HeLa and SAS cells stably transfected with Mock or FLAG-NDRG2 expression vector were subjected to western blotting. The data are representative of three experiments.

Discussion

In this study, we show that NDRG2 interacts with PTEN and promotes its dephosphorylation at Ser380/Thr382/Thr383 by recruiting PP2A to PTEN. We also demonstrated that loss of *NDRG2* expression via genetic or epigenetic abnormalities in ATLL cells can contribute to the increase in PTEN-Ser380/Thr382/Thr383 phosphorylation, which leads to inactivation of PTEN lipid phosphatase activity and activation of the PI3K-AKT

pathway. The imbalance of the expression of *NDRG2* and as yet unidentified protein kinases might account for an elevation of PTEN-Ser380/Thr382/Thr383 phosphorylation with a high amount of phosphorylated AKT in ATLL cells. Finally, we showed that *NDRG2*-deficient mice develop multiple types of tumours, thus establishing that loss of *NDRG2* expression can contribute to tumour development.

PTEN stability and lipid phosphatase activity can be regulated through phosphorylation of the C-terminal tail, which contains a cluster of serine–threonine residues: Ser370, Ser380, Thr382, Thr383 and Ser385 (ref. 35). Although the cluster of Ser380/Thr382/Thr383 residues in the C-terminal tail are thought to be minor phosphorylation sites[26,36], the level of phosphorylated PTEN-Ser380/Thr382/Thr383 has been shown to be rapidly and transiently increased in hypothalamic cells treated with leptin and in rat brains following transient middle cerebral artery occlusion[37,38]. CK2 is known to be a major kinase that phosphorylates PTEN at the C-terminal serine–threonine cluster, but phosphorylation of Ser380/Thr382/Thr383 by CK2 is still under debate[21,26,36,39]. We observed that suppression of CK2 activity with specific inhibitors in ATLL cells did not influence PTEN-Ser380/Thr382/Thr383 phosphorylation. Thus, it is likely that CK2 is not responsible for the phosphorylation of PTEN at Ser380/Thr382/Thr383 in ATLL cells. In contrast, the expression of NDRG2 is markedly upregulated in several tumour cell lines exposed to hypoxic conditions and is thought to be a new hypoxia-inducible factor-1 target gene[40,41]. It could be speculated that *NDRG2* expression is induced by hypoxia-ischemia in the brain to regulate PTEN phosphorylation, leading to the suppression of PI3K-AKT activation and induction of apoptosis. Interestingly, several kinases, including SGK1 (serum- and glucocorticoid-induced kinase 1), PKCθ (protein kinase C-θ) and AKT, have been found to phosphorylate NDRG2 (refs 42,43). These phosphorylation events are likely to affect the cellular function of NDRG2. It is intriguing to speculate that NDRG2 might be a downstream target of the PI3K-AKT signalling pathway that may participate in a negative feedback loop in PI3K-AKT signalling. PP2A exists predominantly as a heterotrimer composed of catalytic C, structural A and one member of four families of regulatory B subunits. The activity, substrate specificity and subcellular localization of the PP2A holoenzyme are thought to be determined by its B subunit[44]. A recent study has shown that following AKT phosphorylation, Clk2 is activated and phosphorylates the PP2A regulatory subunit B56β, thereby leading to the assembly of the PP2A holoenzyme complex on AKT and dephosphorylation of AKT at both Thr308 and Ser473 (ref. 45). Thus, a more complex feedback regulation governing NDRG2 and PP2A activities may exist within the PI3K-AKT pathway. Identifying the PP2A regulatory subunit that interacts with NDRG2 would provide important clues in understanding how the dephosphorylation of PTEN by NDRG2-PP2A is regulated upon AKT activation.

Elevated phosphorylation of PTEN-Ser380/Thr382/Thr383 with high levels of activated AKT is frequently observed in acute myeloid leukaemia (AML) and is associated with poor prognosis[46]. The phosphorylation of Ser380/Thr382/Thr383 is also elevated in human fibromyomatous uteri and may be a contributory factor in the development of uterine leiomyomas[47]. Although it is not known whether these phosphorylation events are attributed to the functional inactivation of *NDRG2*, decreased expression and promoter methylation of the *NDRG2* gene have been reported in various types of cancer, such as liver cancers, gastric cancers, colon cancers and glioblastomas[30,31,48–51]. Therefore, we hypothesize that in ATLL and other types of tumour cells without genetic alterations in the PI3K-AKT pathway, the suppression of *NDRG2* transcription disrupts the negative regulation of PI3K-AKT signalling via sustained PTEN-Ser380/Thr382/Thr383 phosphorylation during tumour development (Fig. 8). The finding that PTEN-Ser380/Thr382/Thr383 is highly phosphorylated in all of the organs of *NDRG2*-deficient mice provides additional evidence that the balance between an unidentified PTEN-Ser380/Thr382/Thr383 kinase(s) and PP2A-NDRG2 activity regulates the phospho rylation status of PTEN-Ser380/Thr382/Thr383 *in vivo*. Therefore, we are currently attempting to identify the protein kinase(s) that target PTEN-Ser380/Thr382/Thr383, which has the potential to be a therapeutic drug target in a variety of cancers, including ATLL.

Because NDRG2 has been shown to have growth inhibitory effects on several malignant cell lines through downregulation of several signalling pathways, including PI3K-AKT, janus kinase-signal transducer and activator of transcription (JAK-STAT) and nuclear factor-kappaB signalling[52,53], one may speculate that the phosphorylation of different proteins involved in these signalling pathways is regulated by the PP2A-NDRG2 complex. Indeed, we observed that the ectopic expression of NDRG2 in ATLL cells causes suppression of JAK-STAT and nuclear factor-kappaB activation (data not shown), although the molecular mechanisms underlying these effects are still being elucidated. We speculate that NDRG2 may have a key role in suppressing different oncogenic signalling pathways in tumourigenesis. In conclusion, this study provides the first functional evidence for a tumour suppressor role of NDRG2 and suggests that NDRG2 is involved in the leukaemogenesis of ATLL. Further investigations of the

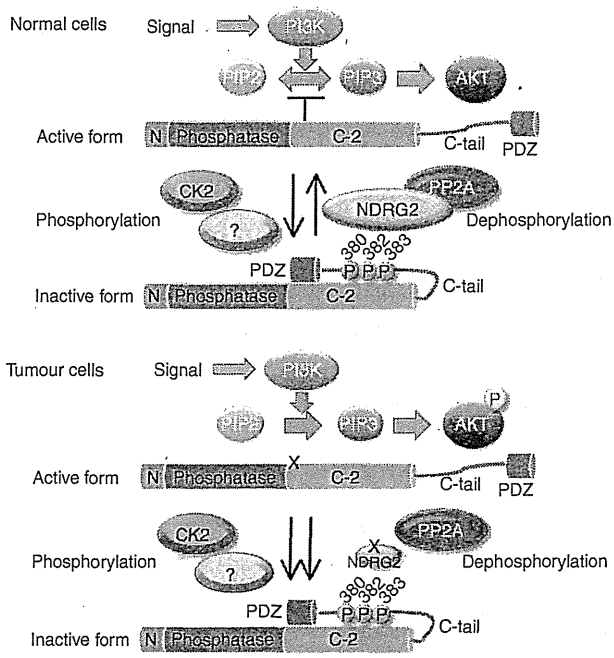

Figure 8 | Schematic model for the regulation of PTEN activity by NDRG2. In normal cells, PP2A is efficiently recruited to PTEN via its interaction with NDRG2, which may facilitate dephosphorylation of PTEN at Ser380/Thr382/Thr383, resulting in an active open conformation of PTEN and subsequently leading to the dephosphorylation of PIP_3 to PIP_2. In tumour cells, expression of NDRG2 is inhibited by DNA methylation of its promoter, causing sustained phosphorylation of PTEN, which keeps PTEN in an inactive closed conformation. Loss of PTEN activity leads to increased PIP_3 levels and AKT activation. The balance between the expression of NDRG2 and an unidentified kinase(s) may have an important role in regulating the phosphorylation status of PTEN.

roles of NDRG2 in the regulation of different signalling pathways may provide clues in understanding the underlying mechanisms of cancer.

Methods

Cell lines. Jurkat, MOLT4, KAWAI and MKB1 are HTLV-1-negative human T-ALL cell lines. KOB, SO4 and KK1 are IL2-dependent ATLL cell lines. ED, Su9T-01 and S1T are IL2-independent ATLL cell lines. MT2, MT4 and HUT102 are human T-cell lines transformed by HTLV-1 infection. Jurkat, MOLT4 and MKB1 were obtained from the Fujisaki Cell Center, Hayashibara Biochemical Laboratories (Okayama, Japan). KAWAI was kindly provided by Dr Y. Hayashi (Gunma Children's Medical Center, Gunma, Japan). MT2, MT4 and HUT102 were kind gifts from Dr H. Iha (Oita University, Oita, Japan). KOB, SO4 and KK1 were kind gifts from Dr Y. Yamada (Nagasaki University, Nagasaki, Japan). Su9T-01 and S1T were kind gifts from Dr N. Arima (Kagoshima University, Kagoshima, Japan). ED was a kind gift from Dr M. Maeda (Kyoto University, Kyoto, Japan). AML cell lines UCSD/AML1, Kasumi-3, K051, NH and MOLM1 were obtained from Dr R. Taetle (VA Medical Center, Sepulveda, CA, USA), from Dr H. Asoh (Hiroshima University, Hiroshima, Japan), from Dr T. Nomura (Nippon Medical School, Tokyo, Japan), from Dr K. Suzukawa (University of Tsukuba, Ibaraki, Japan) and from the Fujisaki Cell Center, Hayashibara Biochemical Laboratories (Okayama, Japan), respectively, and OIH-1 and FKH-1 were obtained from Dr H. Hamaguchi (Musashino Red Cross Hospital). Pancreatic cancer cell lines KLM1, PK9 and PK45P, OSCC cell lines SAS, HO-1-U-1, Ca9-22, HSC2, HSC3, HSC4, HSQ89 and Sa3, cervical cancer cell line HeLa, human embryonic kidney cell line HEK293T and mouse embryonic fibroblast cell line NIH3T3 were obtained from RIKEN Bioresource Center (Tsukuba, Japan). Hepatic cancer cell lines HLF and HuH28 and breast cancer cell line SK-BR-3 were obtained from the Japanese Cancer Research Resources Bank (Tokyo, Japan). Hepatic cancer cell lines HepG2 and HuH7 were obtained from the Health Science Research Resources Bank (Osaka, Japan). Lung cancer cell lines A549, H322, H1395, H1437 and H1648 were obtained from the American Type Culture Collection (Rockville, MD, USA). Glioblastoma cell line A172 and neuroblastoma cell lines NH6 and NH12 were kind gifts from Dr Y. Hayashi (Gunma Children's Medical Center, Gunma, Japan). Prostate cancer cell line PC3 was a kind gift from Dr T. Ochiya (National Cancer Center Research Institute, Tokyo, Japan). Gastric cancer cell lines Mkb28, Mkb45, and KatoIII and ovarian cancer cell line SKOV3 were kind gifts from Dr H. Kataoka (University of Miyazaki, Miyazaki, Japan). IL2-dependent ATLL cell lines were maintained in RPMI 1640 medium (Wako) supplemented with 10% fetal bovine serum and 50 JRU per ml recombinant human IL2 (Takeda). HTLV-1-negative cell lines, cell lines transformed with HTLV-1 and IL2-independent ATLL cell lines were maintained in the same medium without IL2. The other cell lines were cultured in RPMI 1640 or Dulbecco's modified Eagle's medium (Wako) supplemented with 10% fetal bovine serum.

Patient samples. Blood samples were obtained with informed consent with approval by the Institutional Review Board of the Faculty of Medicine, University of Miyazaki. ATLL cells were collected from the patients at the time of hospital admission before the chemotherapy started. The diagnosis of ATLL was based on clinical features, hematological characteristics and the presence of anti-HTLV-1 antibodies in the sera. Monoclonal HTLV-1 provirus integration into the DNA of leukaemic cells was confirmed by Southern blot analysis in all cases. Peripheral blood mononuclear cells (PBMCs) obtained from healthy volunteers and patients with ATLL were purified by gradient centrifugation (Sigma-Aldrich). The procedure for the isolation of ATLL cells from PBMCs has been described elsewhere[54]. $CD4^+$ T cells were purified from PBMCs of healthy volunteers by using anti-CD4 magnetic beads (Miltenyi Biotec) according to the manufacturer's instructions.

Antibodies and reagents. A synthetic peptide (17-PGQTPEAAKTHSVET-31) of human NDRG2 conjugated to keyhole limpet haemocyanin was used for immunization to generate a rabbit polyclonal antibody against NDRG2 (ref. 55). Mouse monoclonal (M2) and rabbit polyclonal (F7425) antibodies against FLAG, and mouse monoclonal antibody (AC-15) against β-actin were purchased from Sigma-Aldrich. Rabbit monoclonal antibodies against PTEN (138G6), phospho-AKT (Ser473) (D9E), phospho-AKT (Thr308) (244F9), phospho-GSK3β (Ser9) (D85E12), GSK3β (27C10), and PP2A C Subunit (PP2Ac) (52F8), rabbit polyclonal antibodies against phospho-PTEN (Ser380/Thr382/383) (9554), non-phospho-PTEN (Ser380/Thr382/383) (9569), AKT (9272), FOXO1/4 (9462) and cleaved caspase-3 (9661), and mouse monoclonal antibodies against PTEN (26H9) and Myc-tag (9B11) were obtained from Cell Signaling Technology. Rabbit polyclonal antibodies against phospho-PTEN (Ser370) (07-889) and PI3K p85 (06-195) were obtained from Upstate/Millipore, rabbit polyclonal antibody against phospho-PTEN (Ser385) (44-1064G) was obtained from Biosource, mouse monoclonal antibody against SHIP1 (P1C1) and goat polyclonal antibody against NDRG2 (E20) were obtained from Santa Cruz Biotechnology, rabbit polyclonal antibody against GFP (598) was obtained from MBL, and rat monoclonal antibodies against mouse B220 (RA3-6B2), mouse CD4 (RM4-5) and mouse CD8 (53-6.7) and hamster monoclonal antibody against mouse CD3 (500A2) were obtained from BD Pharmingen. Mouse monoclonal antibody against TAX (MI73) was a kind gift from Dr M. Matsuoka (Kyoto University, Kyoto, Japan). Recombinant human PP2A core enzyme made up of polyhistidine-tagged (His_{8X}) human PP2Ac and FLAG-tagged human PR65/A co-expressed in baculovirus-infected High Five cell, OA and trichostatin A were obtained from Wako. Dimethyl 3,3′-dithiobispropionimidate (DTBP) was obtained from Thermo Fisher Scientific, and TBB was obtained from Calbiochem. CX-4945 was obtained from Selleckchem, and 5-aza-2'-deoxycytidine was obtained from Sigma-Aldrich.

Plasmid construction. Full-length complementary DNA (cDNA) of *NDRG2* was isolated by RT–PCR from total RNA of the MOLT4 cell line and subcloned into the p3XFLAG-myc-CMV-26 expression vector (Sigma-Aldrich) by standard cloning procedures (FLAG-NDRG2). The FLAG-tagged NDRG2 deletion constructs—NDRG2-deltaN (amino acids 26–357), NDRG2-deltaC (amino acids 1–304), NDRG2-NDR (amino acids 26–304), NDRG2-HD (amino acids 81–297) and NDRG2-Cterm (amino acids 259–357)—were generated by PCR using the NDRG2/pCMV26 as the template and subcloned into p3XFLAG-myc-CMV-26. The GFP-PTEN constructs—GFP-PTEN, GFP-PTEN-N (amino acids 1–185) and GFP-PTEN-C (amino acids 186–403)—were generated by PCR using the PTEN/pcDNA3 (a kind gift from Dr T. Kohno, National Cancer Center Research Institute, Tokyo, Japan) as the template and subcloned into pEGFP-C1 vector (Clontech). A full-length *PTEN* cDNA was amplified from the Su9T-01 cell line by PCR and subcloned into the p3XFLAG-myc-CMV-26. To generate substitution mutant PTEN expression vectors (PTEN-S370A, -S380A/T382A/T383A and -S385A), PCR-based mutagenesis were performed to introduce mutations in the PTEN coding sequence using mutagenic primers listed in Supplementary Table 8 and p3XFLAG-myc-CMV-26/PTEN plasmid as the template. All PCR-generated products were confirmed by nucleotide sequencing. The expression vector for constitutively active PI3K (pmycBD110)[56], which carries the p110-binding domain of p85α attached to the N-terminal region of p110, was kindly provided by Dr Y. Fukui (National Health Research Institutes, Taiwan). The myc-PP1c/pcDNA3, myc-PP2Ac/pcDNA3 and myc-PP5c/pcDNA3 constructs have been described *elsewhere*[57].

Bisulfite sequencing. A 200-ng DNA sample was denatured in 0.2 M NaOH followed by the addition of bisulfite solution (2.5 M sodium bisulfite, 10 mM hydroquinone and 240 mM NaOH). The mixture was then incubated at 55 °C for 16 h. DNA samples were desulfonated in 0.2 M NaOH and precipitated with ethanol. PCR was performed in a 20-μl volume containing 1 μl of bisulfite-treated DNA, 500 μM of dNTP and 500 nM of each primer for the *NDRG2* promoter region (nucleotides 20564110-20563790, GenBank accession no. NC_000014) (forward 5′-TTTTCGAGGGGTATAAGGAGAGTTTATTTT-3′ and reverse 5′-CCAAAAACTCTAACTCCTAAATAAACA-3′) (ref. 48), and 1 unit of Taq polymerase (Takara) under the following conditions: 98 °C for 30 s; 40 cycles of 98 °C for 10 s, 60 °C for 5 s and 72 °C for 30 s; and final extension at 72 °C for 3 min. PCR products were subcloned into the pTA2 vector (TOYOBO) and sequenced.

Real-time RT-PCR analysis. Total RNA was isolated from cells using TRIzol reagent (Invitrogen) and 1 μg of total RNA was reverse transcribed to obtain first-strand cDNA using an RNA-PCR kit (Takara) following the manufacturer's instructions. The resulting cDNA was used for real-time RT–PCR using a SYBR Green PCR Master Mix kit (Applied Biosystems). PCR was performed in a 25-μl volume containing 1 μl cDNA, 300 μM of each primer and 12.5 μl of 2 × PCR master mix under the following conditions: 95 °C for 10 min followed by 40 cycles of 95 °C for 15 s and 60 °C for 1 min. For NDRG2 primers, the cycling conditions were 95 °C for 10 min, 40 cycles of 95 °C for 15 s, 60 °C for 20 s and 72 °C for 40 s. The primers used were as follows: for *PTEN*, PTEN-F (5′-CAGCCATCATCAAA GAGATCG-3′) and PTEN-R (5′-TTGTTCCTGTATACGCCTTCAA-3′); for *NDRG2*, NDRG2-F (5′-CTGGAACAGCTACAACAACC-3′), and NDRG2-R (5′-TCAACAGGAGACCTCCATGG-3′); and for β-actin, ACTB-F (5′-GACAGGA TGCAGAAGGAGATTACT-3′), and ACTB-R (5′-TGATCCACATCTGCTGGA AGGT-3′). The data were normalized to the amount of β-actin mRNA, and the values are represented as the mean ± s.d. of $2^{-\Delta\Delta Ct}$ in a duplicate assay.

Western blot analysis. Cell lysate samples were prepared in NP-40 lysis buffer (50 mM Tris–HCl, pH 8.0, 150 mM NaCl, 5 mM EDTA, 1% NP-40) supplemented with protease inhibitor cocktail (Sigma-Aldrich) and phosphatase inhibitors (PhosStop, Roche) or by direct lysis in boiling Laemmli SDS sample buffer (62.5 mM Tris–HCl, pH 6.8, 2% SDS, 25% glycerol, 5% β-mercaptoethanol and 0.01% bromophenol blue). Protein samples were electrophoresed on 10% SDS-polyacrylamide gel and transferred to polyvinylidine difluoride membranes (Immobilon-P, Millipore). The membranes were blocked in Tris-buffered saline (TBS)-Tween (0.1%) with either 5% bovine serum albumin (BSA) or 5% nonfat dried milk and were then incubated with each primary antibody diluted in TBS containing 0.1% Tween 20 supplemented with either 5% nonfat dried milk or 5% BSA or in the Can Get Signal buffer (TOYOBO). Bound antibody was detected by a Lumi-light Plus kit according to the manufacturer's instructions (Roche Diagnostics). Band intensities on blots were quantified using NIH Image J software. All primary antibodies were used at a dilution of 1:1,000, except anti-β-actin

(1:5,000) and anti-NDRG2 (E20, 1:250). Representative full-gel bots are provided in the Supplementary Fig. 22)

Immunoprecipitation assays. For detecting interaction between endogenous proteins, MOLT4 cells (1×10^7) and mouse frontal cortex tissue were solubilized with RIPA buffer (50 mM Tris–HCl, pH 7.8, 150 mM NaCl, 1% NP-40, 0.25% sodium deoxycholate and 1 mM EDTA) and NP-40 lysis buffer, respectively, supplemented with protease inhibitor cocktail (Sigma-Aldrich) and phosphatase inhibitors (PhosStop, Roche), and the lysates were then incubated with control rabbit immunoglobulin G or antibodies against NDRG2 (rabbit polyclonal, 1:500 or E20, 1:200) or PTEN (26H9, 1:100 or 138G6, 1:300), plus Protein G beads (Amersham Biosciences). After washing, the bound proteins were subjected to SDS-polyacrylamide gel electrophoresis (SDS-PAGE) and immunoblotting with antibodies against NDRG2 (rabbit polyclonal or E20) or PTEN (26H9 or 138G6). For overexpressed proteins, 293T cells were co-transfected with the indicated constructs using HilyMax (Dojindo) according to the manufacturer's instructions. After culturing for 48 h, the transfected cells were solubilized with RIPA buffer, and the lysates were then subjected to immunoprecipitation using FLAG M2 affinity gel (Sigma-Aldrich) or antibodies against GFP (1:200) or PTEN (138G6, 1:500), followed by immunoblotting with antibodies against either FLAG (F7425), GFP or PTEN (26H9). For chemical crosslinking, stable HUT102 or KK1 cell lines expressing FLAG-NDRG2 were washed twice with phosphate-buffered saline (PBS) and incubated with 2 mM DTBP in PBS at room temperature for 30 min. After washing twice with PBS, cells were lysed in TNT buffer (10 mM Tris–HCl, pH 7.5, 150 mM NaCl and 0.5% Triton X-100) supplemented with protease inhibitor cocktail (Sigma-Aldrich) and phosphatase inhibitors (Halt phosphatase inhibitor cocktail, Thermo Scientific), and the lysates were immunoprecipitated with control rabbit immunoglobulin G, antibody against PTEN (138G6, 1:500), or FLAG M2 affinity gel, followed by immunoblotting with antibodies against FLAG (F7425), PP2Ac, PTEN (138G6) or phospho-PTEN (Ser380/Thr382/Thr383).

Immunofluorescence staining. Cells were fixed with 4% paraformaldehyde for 10 min at room temperature, washed with TBS 0.1 M glycine, treated with 0.2% Triton X-100 and rewashed with TBS 0.1 M glycine. After blocking with 1% BSA in TBS, cells were incubated with primary antibodies against NDRG2 (E20, 1:100), FoxO1/4 (1:200), PTEN (138G6, 1:200) or FLAG (M2, 1:500) overnight at 4 °C. The cells were then washed three times with TBS containing 0.1% Tween 20 and incubated with Alexa Fluor-546 anti-mouse, Alexa Fluor-555 anti-rabbit, Alexa Fluor-488 anti-rabbit or Alexa Fluor-488 anti-goat secondary antibodies (Molecular Probes) at room temperature for 2 h. The coverslips were washed three times with TBS containing 0.1% Tween 20 and then mounted on glass slides using an antifade reagent (Invitrogen). Proteins were visualized using a confocal laser scanning microscope (Leica Microsystems). Nuclei were counterstained with 4′,6-diamidino-2-phenylindole (DAPI; Sigma-Aldrich).

RNAi treatment. DNA-based shRNA expression vector (RNAi-Ready pSIREN-RetroQ-ZsGreen vector, Clontech) and siRNA oligonucleotides were used in gene knockdown experiments. The shRNA target sequences were as follows: for human *NDRG2*, shNDRG2#1 (5′-GGTGGAGAGGGCATATGCA-3′) and shNDRG2#2 (5′-GCGAGTCTGGAACTCTTTCTT-3′); for mouse *NDRG2*, 5′-CCGTGAAGA ACAGTGGTAA-3′. A control shRNA vector targeting luciferase (shLuc) was purchased from Clontech. The PP2Acα siRNA (sc-43509) and control siRNA (6568) were purchased from Santa Cruz Biotechnology and Cell Signaling Technology, respectively. The transfections were performed using the Nucleofector V kit (Amaxa) following the company's protocol.

Cell proliferation assays. Cells were seeded onto 96-well microtiter plates at a density of 5×10^3 per well and cultured for the indicated time periods. Viable cells were counted by the methyl thiazolyl tetrazolium assay using a cell counting kit-8 (Dojindo). For stable transfectant cells, cells were seeded into 25 cm^2 flasks at a density of 1×10^5 ml^{-1}, and proliferation rates were assessed by counting the numbers of viable cells every 24 h using Trypan blue staining.

Dephosphorylation assay for synthetic peptides. The PTEN peptide 373-EPDHYRYSDTTDSDPENE-390 and phosphopeptides with pSer380 (EPDHYR-YpSDTTDSDPENE), pThr382 (EPDHYRYSDpTTDSDPENE), pThr383 (EPDHYRYSDTpTDSDPENE) and pSer380/pThr382/pThr383 (EPDHYR-YpSDpTpTDSDPENE) were obtained from TORAY Research Center (Tokyo, Japan). The release of inorganic phosphates from phosphopeptides was determined using a malachite green assay kit (BIOMOL Green reagent, BIOMOL). Cell extracts from the KK1-NDRG2 stable cell line, NIH3T3 cell line and 293T cell line transiently transfected with mock or Myc-tagged PP1c, PP2Ac or PP5c vectors using HilyMax were prepared by lysing cells in TNT buffer supplemented with protease inhibitor cocktail (Sigma-Aldrich). Endogenous PP2Ac and Myc-tagged PP1c, PP2Ac and PP5c were immunoprecipitated using antibodies against anti-PP2Ac (1:500) and anti-Myc (1:500), respectively. For inhibitor treatment, lysates of KK1-NDRG2 cells were incubated on ice for 30 min in the absence or presence of various concentrations of OA. The total cell lysates, immunoprecipitated samples or 0.5 units of recombinant PP2A were incubated with 100 μM PTEN peptide or phosphopeptides in 10 μl of phophatase assay buffer (20 mM HEPES pH 7.0, 1 mM $MnCl_2$, 8 mM $MgCl_2$, 1 mM dithiothreitol and 100 μg ml^{-1} BSA) at 30 °C for 60 min. The reactions were terminated by the addition of 40 μl of TE buffer (10 mM Tris–HCl, pH 8.0, 1 mM EDTA) and 100 μl of BIOMOL Green reagent, and absorbance at 620 nm was determined after incubation for 20 min at room temperature. The quantity of Pi released (nmoles) was calculated based on a standard curve determined for inorganic phosphate according to the manufacturer's recommendations. All assays were performed in duplicate.

PTEN dephosphorylation assay. The KK1-Mock stable cells were lysed in TNT buffer plus protease inhibitor cocktail (Sigma-Aldrich), and the cell lysates were immunoprecipitated with an antibody against PTEN (138G6, 1:500) and Protein G beads. Immunoprecipitates were washed three times with TNT buffer and twice with phosphatase assay buffer, resuspended in phosphatase assay buffer and incubated with 0.5 units of recombinant PP2A for 60 min at 30 °C. The reaction was stopped by adding SDS sample buffer, and the samples were separated by 10% SDS-PAGE, followed by western blotting with antibodies against PTEN (138G6) or phospho-PTEN (Ser370 or Ser380/Thr382/Thr383).

Generation of *NDRG2* knockout mice. *NDRG2*-deficient mice were generated in the Laboratory for Animal Resources and Genetic Engineering, RIKEN Center for Developmental Biology (accession. no. CDB0768K: http://www.cdb.riken.jp/arg/mutant%20mice%20list.html). For generating a targeting vector, genomic fragments for *NDRG2* were obtained from RP23-109J8 BAC clone (BACPAC Resources). A *lacZ*-pA-*neo*-pA cassette was inserted into exon 2 of the *NDRG2* gene to create the targeting construct. The linearized targeting vector was inserted into TT2 ES cells[58] by electroporation, and G418-resistant clones were screened for homologous recombination by PCR and Southern blot analysis using a 457-bp 5′ fragment as the probe. Targeted ES clones were microinjected into ICR eight-cell stage embryos and transferred into pseudopregnant ICR females (http://www.cdb.riken.jp/arg/Methods.html). The resulting chimeras were bred with C57BL/6 mice, and heterozygous offspring were identified by Southern blot analysis and by PCR using the following two primer pairs: WT allele, F1 (5′-CAAACACCCGA GACTGCCAA-3′)/R (5′-ATTAAACAATAAAGATGTCC-3′); targeted-allele, F2 (5′-GACAGGAGAGGATGAAGGTT-3′)/R. Heterozygous mice were backcrossed with C57BL/6 for two generations and mated in the same generation to obtain homozygous mutants. All animal experiments were approved by the Animal Experiment Review Board of the University of Miyazaki.

Histological analysis. All necropsies and histological examinations were performed on mice at the time of death. Tissues were fixed in 10% buffered formalin solution and embedded in paraffin blocks, and 2-μm-thick sections were prepared. Paraffinized sections were deparaffinized with xylene and rehydrated through a decreasing gradient of ethanol solutions. Slides were stained with hematoxylin and eosin (H&E), coverslipped with mounting medium, and viewed under a light microscope. The slides were scanned with a digital scanner (MIRAX; Carl Zeiss) and viewed with MIRAX software (Carl Zeiss). For immunohistochemistry, the tissue sections were deparaffinized and rehydrated. After microwave treatment for 20 min in citrate buffer pH 6.0 and cooling, endogenous peroxidase activity was blocked in 0.3% hydrogen peroxide in methanol for 30 min. After blocking in 5% skim milk in PBS for 30 min, sections were incubated with antibodies against CD3, CD4, CD8, B220, FLAG or cleaved caspase-3 for 60 min at 37 °C, washed three times with PBS and incubated with horseradish peroxidase-conjugated secondary antibodies for 30 min at 37 °C. The horseradish peroxidase activity was visualized with 3, 3′-diaminobenzidine containing hydrogen peroxide. All primary antibodies were used at 1:200 dilution, except anti-FLAG (1:500) and anti-cleaved caspase-3 (1:100).

Statistical analysis. Bars and markers in the figures represent the mean ± s.d. The two-tailed Student's *t*-test and Mann–Whitney *U*-test were used as appropriate. In the Kaplan–Meier survival analysis, the log-rank test was used for analysis. Fisher's exact analysis was used to determine differences in tumour incidence. Differences were considered significant when the *P* value was <0.05, as indicated in the text.

References

1. Takatsuki, K. *et al.* Clinical diversity in adult T-cell leukemia-lymphoma. *Cancer Res.* **45**, 4644s–4645s (1985).
2. Proietti, F. A., Carneiro-Proietti, A. B., Catalan-Soares, B. C. & Murphy, E. L. Global epidemiology of HTLV-I infection and associated diseases. *Oncogene* **24**, 6058–6068 (2005).
3. Yasunaga, J. & Matsuoka, M. Leukaemogenic mechanism of human T-cell leukaemia virus type I. *Rev. Med. Virol.* **17**, 301–311 (2007).
4. Fukuda, R. *et al.* Alteration of phosphatidylinositol 3-kinase cascade in the multilobulated nuclear formation of adult T cell leukemia/lymphoma (ATLL). *Proc. Natl Acad. Sci. USA* **102**, 15213–15218 (2005).

5. Ikezoe, T. *et al.* Longitudinal inhibition of PI3K/Akt/mTOR signaling by LY294002 and rapamycin induces growth arrest of adult T-cell leukemia cells. *Leuk. Res.* **31,** 673–682 (2007).
6. Li, J. *et al.* PTEN, a putative protein tyrosine phosphatase gene mutated in human brain, breast, and prostate cancer. *Science* **275,** 1943–1947 (1997).
7. Steck, P. A. *et al.* Identification of a candidate tumour suppressor gene, MMAC1, at chromosome 10q23.3 that is mutated in multiple advanced cancers. *Nat. Genet.* **15,** 356–362 (1997).
8. Hollander, M. C., Blumenthal, G. M. & Dennis, P. A. PTEN loss in the continuum of common cancers, rare syndromes and mouse models. *Nat. Rev. Cancer* **11,** 289–301 (2011).
9. Ali, I. U., Schriml, L. M. & Dean, M. Mutational spectra of PTEN/MMAC1 gene: a tumor suppressor with lipid phosphatase activity. *J. Natl Cancer Inst.* **91,** 1922–1932 (1999).
10. Cully, M., You, H., Levine, A. J. & Mak, T. W. Beyond PTEN mutations: the PI3K pathway as an integrator of multiple inputs during tumorigenesis. *Nat. Rev. Cancer* **6,** 184–192 (2006).
11. Song, M. S., Salmena, L. & Pandolfi, P. P. The functions and regulation of the PTEN tumour suppressor. *Nat. Rev. Mol. Cell Biol.* **13,** 283–296 (2012).
12. Trotman, L. C. *et al.* Ubiquitination regulates PTEN nuclear import and tumor suppression. *Cell* **128,** 141–156 (2007).
13. Wang, X. *et al.* NEDD4-1 is a proto-oncogenic ubiquitin ligase for PTEN. *Cell* **128,** 129–139 (2007).
14. Maddika, S. *et al.* WWP2 is an E3 ubiquitin ligase for PTEN. *Nat. Cell Biol.* **13,** 728–733 (2002).
15. Vazquez, F., Ramaswamy, S., Nakamura, N. & Sellers, W. R. Phosphorylation of the PTEN tail regulates protein stability and function. *Mol. Cell Biol.* **20,** 5010–5018 (2000).
16. Vazquez, F. *et al.* Tumor suppressor PTEN acts through dynamic interaction with the plasma membrane. *Proc. Natl Acad. Sci. USA* **103,** 3633–3638 (2006).
17. Odriozola, L., Singh, G., Hoang, T. & Chan, A. M. Regulation of PTEN activity by its carboxyl-terminal autoinhibitory domain. *J. Biol. Chem.* **282,** 23306–23315 (2007).
18. Rahdar, M. *et al.* A phosphorylation-dependent intramolecular interaction regulates the membrane association and activity of the tumor suppressor PTEN. *Proc. Natl Acad. Sci. USA* **106,** 480–485 (2009).
19. Silva, A. *et al.* PTEN posttranslational inactivation and hyperactivation of the PI3K/Akt pathway sustain primary T cell leukemia viability. *J. Clin. Invest.* **118,** 3762–3774 (2008).
20. Yang, Z. *et al.* Reduced expression of PTEN and increased PTEN phosphorylation at residue Ser380 in gastric cancer tissues: A novel mechanism of PTEN inactivation. *Clin. Res. Hepatol. Gastroenterol.* **37,** 72–79 (2013).
21. Torres, J. & Pulido, R. The tumor suppressor PTEN is phosphorylated by the protein kinase CK2 at its C terminus. Implications for PTEN stability to proteasome-mediated degradation. *J. Biol. Chem.* **276,** 993–998 (2001).
22. Hidaka, T. *et al.* Down-regulation of TCF8 is involved in the leukemogenesis of adult T-cell leukemia/lymphoma. *Blood* **112,** 383–393 (2008).
23. Popescu, N. C. Genetic alterations in cancer as a result of breakage at fragile sites. *Cancer Lett.* **192,** 1–17 (2003).
24. Yao, L., Zhang, J. & Liu, X. NDRG2: a Myc-repressed gene involved in cancer and cell stress. *Acta Biochim. Biophys. Sin. (Shanghai)* **40,** 625–635 (2008).
25. Fernandes, S., Iyer, S. & Kerr, W. G. Role of SHIP1 in cancer and mucosal inflammation. *Ann. NY Acad. Sci.* **1280,** 6–10 (2013).
26. Al-Khouri, A. M., Ma, Y., Togo, S. H., Williams, S. & Mustelin, T. Cooperative phosphorylation of the tumor suppressor phosphatase and tensin homologue (PTEN) by casein kinases and glycogen synthase kinase 3beta. *J. Biol. Chem.* **280,** 35195–35202 (2005).
27. Qu, X. *et al.* Characterization and expression of three novel differentiation-related genes belong to the human NDRG gene family. *Mol. Cell. Biochem.* **229,** 35–44 (2002).
28. Bialojan, C. & Takai, A. Inhibitory effect of a marine-sponge toxin, okadaic acid, on protein phosphatases, specificity and kinetics. *Biochem. J.* **256,** 283–290 (1988).
29. Hu, X. L. *et al.* Expression analysis of the NDRG2 gene in mouse embryonic and adult tissues. *Cell Tissue Res.* **325,** 67–76 (2006).
30. Lee, D. C. *et al.* Functional and clinical evidence for NDRG2 as a candidate suppressor of liver cancer metastasis. *Cancer Res.* **68,** 4210–4220 (2008).
31. Chang, X. *et al.* DNA methylation of NDRG2 in gastric cancer and its clinical significance. *Dig. Dis. Sci.* **58,** 715–723 (2013).
32. Furuta, H. *et al.* NDRG2 is a candidate tumor-suppressor for oral squamous-cell carcinoma. *Biochem. Biophys. Res. Commun.* **391,** 1785–1791 (2010).
33. Mavros, A. *et al.* Infrequent genetic alterations of the tumor suppressor gene PTEN/MMAC1 in squamous cell carcinoma of the oral cavity. *J. Oral Pathol. Med.* **31,** 270–276 (2002).
34. Kozaki, K. *et al.* PIK3CA mutation is an oncogenic aberration at advanced stages of oral squamous cell carcinoma. *Cancer Sci.* **97,** 1351–1358 (2006).
35. Leslie, N. R., Batty, I. H., Maccario, H., Davidson, L. & Downes, C. P. Understanding PTEN regulation: PIP2, polarity and protein stability. *Oncogene* **27,** 5464–5476 (2008).
36. Miller, S. J., Lou, D. Y., Seldin, D. C., Lane, W. S. & Neel, B. G. Direct identification of PTEN phosphorylation sites. *FEBS Lett.* **528,** 145–153 (2002).
37. Omori, N. *et al.* Enhanced phosphorylation of PTEN in rat brain after transient middle cerebral artery occlusion. *Brain. Res.* **954,** 317–322 (2002).
38. Ning, K. *et al.* A novel leptin signalling pathway via PTEN inhibition in hypothalamic cell lines and pancreatic beta-cells. *EMBO J.* **25,** 2377–2387 (2006).
39. Maccario, H., Perera, N. M., Davidson, L., Downes, C. P. & Leslie, N. R. PTEN is destabilized by phosphorylation on Thr366. *Biochem. J.* **405,** 439–444 (2007).
40. Wang, L. *et al.* NDRG2 is a new HIF-1 target gene necessary for hypoxia-induced apoptosis in A549 cells. *Cell. Physiol. Biochem.* **21,** 239–250 (2008).
41. Liu, J. *et al.* HIF-1 and NDRG2 contribute to hypoxia-induced radioresistance of cervical cancer Hela cells. *Exp. Cell Res.* **316,** 1985–1993 (2010).
42. Burchfield, J. G. *et al.* Akt mediates insulin-stimulated phosphorylation of Ndrg2: evidence for cross-talk with protein kinase C theta. *J. Biol. Chem.* **279,** 18623–18632 (2004).
43. Murray, J. T. *et al.* Exploitation of KESTREL to identify NDRG family members as physiological substrates for SGK1 and GSK3. *Biochem. J.* **384,** 477–488 (2004).
44. Eichhorn, P. J., Creyghton, M. P. & Bernards, R. Protein phosphatase 2A regulatory subunits and cancer. *Biochim. Biophys. Acta* **1795,** 1–15 (2009).
45. Rodgers, J. T., Vogel, R. O. & Puigserver, P. Clk2 and B56β mediate insulin-regulated assembly of the PP2A phosphatase holoenzyme complex on Akt. *Mol. Cell* **41,** 471–479 (2011).
46. Cheong, J. W. *et al.* Phosphatase and tensin homologue phosphorylation in the C-terminal regulatory domain is frequently observed in acute myeloid leukaemia and associated with poor clinical outcome. *Br. J. Haematol.* **122,** 454–456 (2003).
47. Kovács, K. A. *et al.* Phosphorylation of PTEN (phosphatase and tensin homologue deleted on chromosome ten) protein is enhanced in human fibromyomatous uteri. *J. Steroid Biochem. Mol. Biol* **103,** 196–199 (2007).
48. Lusis, E. A. *et al.* Integrative genomic analysis identifies NDRG2 as a candidate tumor suppressor gene frequently inactivated in clinically aggressive meningioma. *Cancer Res.* **265,** 7121–7126 (2005).
49. Tepel, M. *et al.* Frequent promoter hypermethylation and transcriptional downregulation of the NDRG2 gene at 14q11.2 in primary glioblastoma. *Int. J. Cancer* **123,** 2080–2086 (2008).
50. Piepoli, A. *et al.* Promoter methylation correlates with reduced NDRG2 expression in advanced colon tumour. *BMC Med. Genomics* **2,** doi:10.1186/1755-8794-2-11 (2009).
51. Barreau, O. *et al.* Identification of a CpG island methylator phenotype in adrenocortical carcinomas. *J Clin. Endocrinol. Metab.* **98,** E174–E184 (2013).
52. Kim, A. *et al.* Suppression of NF-kappaB activity by NDRG2 expression attenuates the invasive potential of highly malignant tumor cells. *Carcinogenesis* **30,** 927–936 (2009).
53. Park, Y. *et al.* SOCS1 induced by NDRG2 expression negatively regulates STAT3 activation in breast cancer cells. *Biochem. Biophys. Res. Commun.* **363,** 361–367 (2007).
54. Nakahata, S. *et al.* Clinical significance of CADM1/TSLC1/IgSF4 expression in adult T-cell leukemia/lymphoma. *Leukemia* **26,** 1238–1246 (2012).
55. Mitchelmore, C. *et al.* NDRG2: a novel Alzheimer's disease associated protein. *Neurobiol. Dis.* **16,** 48–58 (2004).
56. Kobayashi, M. *et al.* Expression of a constitutively active phosphatidylinositol 3-kinase induces process formation in rat PC12 cells. Use of Cre/loxP recombination system. *J. Biol. Chem.* **272,** 16089–16092 (1997).
57. Sugiyama, K. *et al.* Aurora-B associated protein phosphatases as negative regulators of kinase activation. *Oncogene* **21,** 3103–3111 (2002).
58. Yagi, T. *et al.* A novel ES cell line, TT2, with high germline-differentiating potency. *Anal. Biochem.* **214,** 70–76 (1993).

Acknowledgements

We thank Y. Motoyoshi, A. Nakatake and I. Morinaga for their technical assistance and N. Ishigami for secretarial assistance. We thank all of the members of the Division of Tumor and Cellular Biochemistry and HTLV-1/ATL Research Facility, University of Miyazaki for helpful discussions and comments. Also, we gratefully thank all of the researchers, who kindly provided us their important cell lines and materials. This work was supported by Grant-in-Aid for Scientific Research on Priority Areas (20012043) from the Ministry of Education, Culture, Sports, Science and Technology (*MEXT*) of Japan; Research fund from Miyazaki Prefecture Collaboration of Regional Entities for the Advancement of Technological Excellence (60G01-B7002022), Japan Science and Technology Agency (JST); Scientific Research (B) (21390098) (KM); and Young Scientists (B) (23701061 to SN and 23790372 to TI) of Japan Society for the Promotion of Science (JSPS).

Author contributions

S.N., T.I. and K.M. designed the research; S.N., T.I., M.H., N.Y. and Y.A. performed the experiments and analysed the results; P.M., T.T., K.O., N.M. and R.Y. performed the

histopathology; Y.S., K.N., T.T. and M.T. performed the SNP array analysis; T.A. and H.K. generated *NDRG2*-deficient mice; M.H. and K.N. performed the cDNA microarray analysis; K.N. and Y.K. performed the DNA methylation array analysis; K.S. provided patient samples; I.K. Y.A., T.T., A.H., and H.S. edited and commented on the manuscripts; S.N. and K.M. wrote the manuscript; K.M. supervised the project.

Additional information

Accession codes: The gene expression data have been deposited in the Gene Expression Omnibus database under accession code GSE43017.

Supplementary Information accompanies this paper at http://www.nature.com/naturecommunications

Competing financial interests: The authors declare no competing financial interests.

Reprints and permission information is available online at http://npg.nature.com/reprintsandpermissions/

How to cite this article: Nakahata, S. *et al.* Loss of NDRG2 expression activates PI3K-AKT signalling via PTEN phosphorylation in ATLL and other cancers. *Nat. Commun.* 5:3393 doi: 10.1038/ncomms4393 (2014).

Leukemia (2013) 27, 1637–1649

www.nature.com/leu

ORIGINAL ARTICLE

Maintenance of the hematopoietic stem cell pool in bone marrow niches by EVI1-regulated GPR56

Y Saito[1], K Kaneda[1], A Suekane[1], E Ichihara[1], S Nakahata[1], N Yamakawa[1], K Nagai[1], N Mizuno[2], K Kogawa[3], I Miura[4], H Itoh[2] and K Morishita[1]

Acute myeloid leukemia with high ecotropic viral integration site-1 expression (EVI1^{high} AML) is classified as a refractory type of leukemia with a poor prognosis. To provide new insights into the prevention and treatment of this disease, we identified the high expression of EVI1-regulated G protein-coupled receptor 56 (GPR56), and the association of high cell adhesion and antiapoptotic activities in EVI1^{high} AML cells. Knockdown of GPR56 expression decreased the cellular adhesion ability through inactivation of RhoA signaling, resulting in a reduction of cellular growth rates and enhanced apoptosis. Moreover, in *Gpr56*$^{-/-}$ mice, the number of hematopoietic stem cells (HSCs) was significantly decreased in the bone marrow (BM) and, conversely, was increased in the spleen, liver and peripheral blood. The number of *Gpr56*$^{-/-}$ HSC progenitors in the G0/G1-phase was significantly reduced and was associated with impaired cellular adhesion. Finally, the loss of GPR56 function resulted in a reduction of the *in vivo* repopulating ability of the HSCs. In conclusion, GPR56 may represent an important GPCR for the maintenance of HSCs by acting as a co-ordinator of interactions with the BM osteosteal niche; furthermore, this receptor has the potential to become a novel molecular target in EVI1^{high} leukemia.

Leukemia (2013) **27,** 1637–1649; doi:10.1038/leu.2013.75

Keywords: acute myeloid leukemia; EVI1; GPR56; hematopoietic stem cell; RhoA

INTRODUCTION

Acute myeloid leukemia (AML) is a cancer of the myeloid line of blood cells, and refractory AML is considered a stem cell disease. Leukemia stem cells (LSCs) are thought to be the hijack maintenance mechanisms of hematopoietic stem cells (HSCs) in the bone marrow (BM), and consequently to contribute to eventual disease relapse after they have survived undetected in the BM niche during chemotherapy.[1,2] Therefore, if the adhesion molecules specific for LSC maintenance in the BM niche can be found, targeting these interaction molecules between LSC and the surrounding support cells could represent a promising and novel therapeutic strategy for AML.

The ecotropic viral integration site-1 (EVI1) transcription factor is a well-known marker of poor prognosis for chemotherapy-resistant AML.[3–8] The gene expression profiles found in acute myeloid leukemia with high ecotropic viral integration site-1 expression (EVI1^{high} AML) patients are quite similar to those of BM CD34^{+} cells;[9,10] EVI1 is implicated in stem cell regulation and oncogenesis, and contributes to the poor clinical outcome of AML by promoting stemness.[11] EVI1 maintains the self-renewal capacity of embryonic HSCs by activating Gata2 transcription,[12] and the ablation of EVI1 in adult BM leads to a significant decrease in the numbers of HSCs.[13] Therefore, EVI1 may have an important role in the maintenance of cell quiescence and stem cell-like phenotypes in leukemia cells, thereby contributing to their chemoresistance.

To identify novel therapeutic molecules targeting EVI1^{high} AML cells, we analyzed the gene expression profiles of these molecules and the newly identified G protein-coupled receptor 56 (GPR56) as a candidate target molecule for EVI1^{high} AML cells, along with CD52, integrin α6 and Angiopoietin-1.[14–16] GPR56 is a member of the secretin family and has been linked to developmental malformations of the human brain, known as bilateral frontoparietal polymicrogyria.[17–19] GPR56, coupled with $G\alpha_{12/13}$, induces Rho-dependent activation of transcription, resulting in actin fiber reorganization and inhibition of neural progenitor cell migration.[20] In cancer cells, overexpression of GPR56 can suppress tumor growth and metastasis in melanoma cell lines, and GPR56 functions in tumor cell adhesion in glioma cells.[21–23] Although the function of GPR56 in HSCs is still unknown,[24] GPR56 was also identified in a family of LSC-related genes correlated with a worse prognosis of AML.[11] GPR56 regulates RhoA signaling involved in cellular adhesion, and the small GTPases Rac and Cdc42 control HSC adhesion, migration and mobilization in BM niches;[25–30] therefore, we speculated that GPR56 has an important role in the maintenance of HSCs and/or LSCs in the BM niche.

In this study, we found that GPR56 was specifically expressed in EVI1^{high} AML cells as an EVI1-targeted gene and was associated with high cell adhesion and antiapoptotic activities in the leukemia cells. To further define the role of GPR56 in HSC regulation, we analyzed the function of HSCs in *Gpr56*$^{-/-}$ mice, and our results demonstrated a role of Gpr56 in maintaining HSC quiescence and osteosteal niche interactions in the BM. Because the expression of GPR56 in LSCs is higher than in HSCs, GPR56 has potential as a novel therapeutic target for EVI1^{high} AML.

[1]Division of Tumor and Cellular Biochemistry, Department of Medical Science, Faculty of Medicine, University of Miyazaki, Miyazaki, Japan; [2]Laboratory of Molecular Signal Transduction, Graduate School of Biological Sciences, Nara Institute of Science and Technology, Nara, Japan; [3]Department of Pediatrics, National Defense Medical College, Tokorozawa, Japan and [4]Division of Hematology and Oncology, Department of Internal Medicine, St Marianna University School of Medicine, Kawasaki, Japan. Correspondence: Dr K Morishita, Division of Tumor and Cellular Biochemistry, Department of Medical Science, Faculty of Medicine, University of Miyazaki, 5200 Kihara, Kiyotake, Miyazaki 889-1692, Japan.
E-mail: kmorishi@med.miyazaki-u.ac.jp
Received 15 October 2012; revised 4 March 2013; accepted 6 March 2013; accepted article preview online 12 March 2013; advance online publication, 5 April 2013

MATERIALS AND METHODS

Cell lines

UCSD/AML1 and HNT34 cells were cultured in RPMI1640 (Roswell Park Memorial Institute medium) supplemented with 10% fetal calf serum and 1 ng/ml of human granulocyte-macrophage (GM) colony-stimulating factor. U937 and K562 cells were cultured in RPMI1640 supplemented with 10% fetal calf serum, and 293T cells were cultured in Dulbecco's modified eagle medium supplemented with 10% fetal calf serum. Detailed information concerning our cell lines is available as described previously.[14]

Patient samples

Leukemia cells were obtained from AML patients before chemotherapy. A summary of the AML patient samples used in this study is presented in Supplementary Table 1. One sample with high expression of EVI1, consisting of PT9 cells, was cultured in RPMI1640 supplemented with 10% fetal calf serum and 1 ng/ml granulocyte-macrophage colony-stimulating factor.[14] This study was approved by the Institutional Review Board of the Faculty of Medicine of the University of Miyazaki. Informed consent was obtained from all donors in accordance with the Declaration of Helsinki.

Quantitative real-time reverse-transcription PCR

After extraction of total RNA using the TRIzol reagent (Invitrogen, Carlsbad, CA, USA), 1 μg of total RNA was reverse transcribed to produce complementary DNA using Reverse Transcriptase XL (AMV, avian myeloblastosis virus) (Takara-Bio Inc., Tokyo, Japan). The resulting first-strand complementary DNA was used as a template for real-time PCR. Real-time PCR was performed using MESA GREEN qPCR MasterMix Plus for SYBR assay (EUROGENTEC, Seraing, Belgium). The primers used in these experiments are listed in Supplementary Table 2. The mRNA expression levels of several genes were detected using an *ABI Prism 7000* (Applied Biosystems, Foster City, CA, USA), and the data obtained were analyzed with Sequence Detection System software (Applied Biosystems) and normalized to β-actin.

Mice

Gpr56$^{-/-}$ mice were kindly provided by Genentech (South San Francisco, CA, USA).[18,19,31] C57BL/6 CD45.1 congenic mice (B6-CD45.1) were purchased from Sankyo-Lab Service (Tsukuba, Japan). For analysis of blood counts, peripheral blood (PB) from the tail vein was collected in a heparinized microtube and analyzed on a hematology analyzer (CellTac, NIHON KOHDEN, Tokyo, Japan).

Isolation of murine HSCs and flow cytometry

BM was collected from femurs and tibiae. Lin$^+$ cells were removed by immunomagnetic selection using AutoMACS magnetic-activated cell separation (Auto MACS, Miltenyi Biotec, Bergisch, Gladbach, Germany). Lin$^-$ cells were enriched for cells expressing c-Kit using Miltenyi CD117 microbeads and an AutoMACS magnetic selection device. The HSCs and myeloid progenitors were sorted by first staining Lin$^-$ BM cells with Alexa Fluor 647-conjugated anti-CD34 (RAM34; BD Bioscience, Franklin Lakes, NJ, USA), PerCP-Cy5.5-conjugated anti-CD16/32 (93; eBioscience, San Diego, CA, USA), PE-Cy5-conjugated anti-Flk2 (A2F10; eBioscience) and biotinylated anti-mGpr56 antibodies, followed by streptavidin-Allophycocyanin (APC)/Cy7 (BioLegend, San Diego, CA, USA). A rabbit anti-mGpr56 antibody was used as described previously.[20] Cells were then sorted using a JSAN cell sorter (Bay bioscience, Kobe, Japan).

RESULTS

High expression of GPR56 in EVI1^{high} AML cells

To search for novel molecular targets for EVI1^{high} AML, we recently analyzed the gene expression profiles of 12 human myeloid cell lines using an oligonucleotide microarray; from this analysis, GPR56 was identified.[14,15] In the present study, we focused on the analysis of GPR56, an orphan G protein-coupled receptor. Initially, we used quantitative real-time PCR to measure the expression of *EVI1* and *GPR56* in a panel of leukemia cell lines and primary leukemia samples (Figures 1a and b). Our results revealed that *GPR56* mRNA was significantly more highly expressed in the EVI1^{high} leukemia cell lines and patient samples than in their EVI1^{low} counterparts ($P<0.05$), and the expression of *GPR56* was highly correlated with the expression of *EVI1* (Figures 1a and b). Furthermore, based on gene expression profiles from a large number of patients with AML ($n=460$) (accession number GSE6891),[10] *GPR56* was highly expressed in EVI1^{high} AML cells compared with EVI1^{low} AML cells (Supplementary Figure 1a). In addition, the *GPR56* mRNA level associated with intermediate- and high-risk AML samples was significantly higher than that in the low-risk AML samples (Supplementary Figure 1b), suggesting that *GPR56* expression is a marker of poor prognosis in AML patients.

The expression of GPR56 was regulated by the EVI1 transcription factor

To determine whether the expression of *GPR56* is regulated by EVI1, we introduced an expression vector for EVI1-specific (shEVI1) or non-specific small hairpin RNA (shCNTL) into EVI1^{high} UCSD/AML1 and PT9 cells to establish UCSD/AML1 and PT9 cells exhibiting EVI1^{low} expression (UCSD/AML1/shEVI1, PT9/shEVI1) and control cells (UCSD/AML1/shCNTL, PT9/shCNTL). The expression of *GPR56* was significantly reduced in the UCSD/AML1/shEVI1 and PT9/shEVI1 cells compared with *GPR56* expression in parental and control cells (Figures 1c–e and Supplementary Figure 2). By contrast, the introduction of an EVI1 expression vector into U937 cells expressing EVI1^{low} produced U937 cells showing EVI1^{high} expression (U937/EVI1). The expression of *GPR56* was significantly increased in U937/EVI1 cells compared with control parental and U937/Mock cells (Figures 1f–h). To determine whether EVI1 regulates GPR56 expression, we next isolated a 3-kb fragment from the genomic promoter region of *GPR56* and inserted it in front of the firefly luciferase gene (pGL4-3.0). We created promoter DNA deletion mutants by deleting the region up to −1.5 (pGL4-1.5) or −2.4 (pGL4-2.4) kb, and the promoter activity was determined via luciferase assays after transfection into COS7 cells (Figure 2a). We found that the region between −2.4 and −3.0 kb markedly enhanced the promoter activity of *GPR56* in the presence of transfected EVI1. In addition, a possible binding sequence for the second DNA-binding domain of EVI1, GAAGAT, was found in the region between −2.4 and −3.0 kb. This binding sequence was replaced with the nucleotide sequence CCCGAC in the pGL4-3.0 plasmid (pGL4-3.0 m), and the resultant mutant plasmid completely abolished *GPR56* transcriptional activity. To confirm the DNA-binding activity of EVI1, several EVI1 deletion mutants were transfected into COS7 cells, and their *GPR56* transcriptional activity was measured (Figure 2b). The transcriptional activity of the mutant containing a deletion of the repression domain (ΔRD) showed less than half of the wild-type activity, and deletion of the second DNA-binding domain along with the eighth through the tenth zinc finger repeats (ΔD2 (8–10)) completely abolished *GPR56* transcriptional activity. In addition, the ΔD2 (8–10) EVI1 mutant protein was not precipitated by the DNA fragment of the GPR56 promoter region in chromatin immunoprecipitation assays (Figure 2c). Finally, the endogenous EVI1 protein was precipitated from UCSD/AML1 cells using the same GPR56 promoter region with the EVI1-binding site via chromatin immunoprecipitation with an anti-EVI1 antibody (Figure 2d). Therefore, EVI1 binds directly to the promoter region of *GPR56* and regulates *GPR56* expression in EVI1^{high} leukemia cells.

GPR56 regulated cell adhesion and migration in EVI1^{high} AML cells

Because high expression of GPR56 promotes tumorigenesis by enhancing the cellular adhesion of glioma cells,[21] we next compared the cell migration and adhesion abilities of leukemia

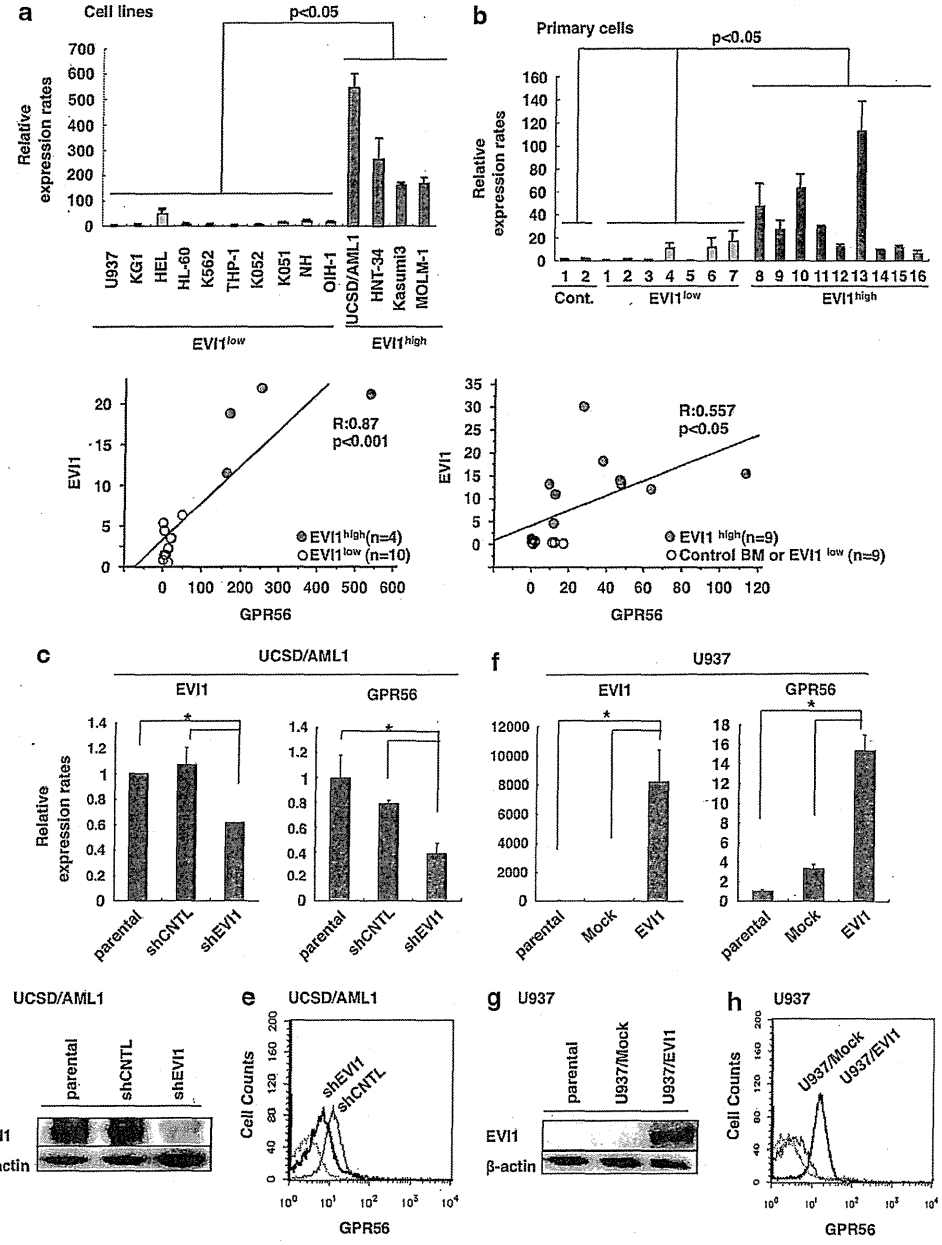

Figure 1. GPR56 is highly expressed in EVI1^{high} leukemia cells. (**a**) *GPR56* was detected in 14 AML cell lines, including 10 EVI1^{low} and 4 EVI1^{high} AML cell lines, using quantitative real-time PCR. The data are shown as the fold change in *GPR56* mRNA expression (normalized to β-actin) relative to *GPR56* expression in U937 cells. The data are presented as the means ± s.d.. The lower figure shows the correlation between the expression of EVI1 and GPR56 in the EVI1^{high} and EVI1^{low} AML cell lines based on quantitative real-time PCR analysis. The significance of the differences among the groups was assessed via a two-tailed Student's *t*-test. (**b**) *GPR56* was detected in 16 primary AML cell samples, including seven EVI1^{low} and nine EVI1^{high} AML samples. Two BM samples from healthy volunteers were used as controls. The data are shown as the fold changes in *GPR56* mRNA expression (normalized to β-actin) relative to the *GPR56* expression in control BM cells (no. 1). The data are presented as the means ± s.d. The lower figure shows the correlation between the expression of EVI1 and GPR56 in EVI1^{high} and EVI1^{low} primary AML cells and control BM samples based on quantitative real-time PCR analysis. The significance of the differences among the groups was assessed via a two-tailed Student's *t*-test. (**c**) Introduction of the small hairpin RNA (shRNA) expression vector specific for EVI1 into UCSD/AML1 cells with EVI1^{high} expression decreased GPR56 expression. Quantitative real-time reverse-transcription PCR (RT-PCR) analysis of EVI1 and GPR56 was performed in parental cells, shCNTL cells, and shEVI1 cells. The data were normalized to β-actin and are presented as relative fold changes compared with the expression in parental UCSD/AML1 cells. The data are presented as the means ± s.d. (**d**) The expression of EVI1 was downregulated in the UCSD/AML1/shEVI1 cells. EVI1 protein expression in parental UCSD/AML1, UCSD/AML1/shCNTL and UCSD/AML1/shEVI1 cells was detected using an anti-EVI1 antibody. (**e**) The cell surface expression of GPR56 in UCSD/AML1/shCNTL and UCSD/AML1/shEVI1 cells was detected by flow cytometric analysis. (**f**) The induction of GPR56 expression by forced expression of EVI1 in U937 cells expressing EVI1^{low} is shown. Quantitative real-time RT-PCR analysis of EVI1 and GPR56 was performed in parental U937 cells, U937/Mock cells and U937/EVI1 cells. The data were normalized to β-actin and are presented as relative fold changes compared with the expression in parental U937 cells. The data are presented as the means ± s.d. (**g**) EVI1 protein expression in parental U937 cells, U937/Mock cells and U937/EVI1 cells was detected with an anti-EVI1 antibody. (**h**) The cell surface expression of GPR56 in U937/Mock cells and U937/EVI1 cells was detected by flow cytometric analysis.

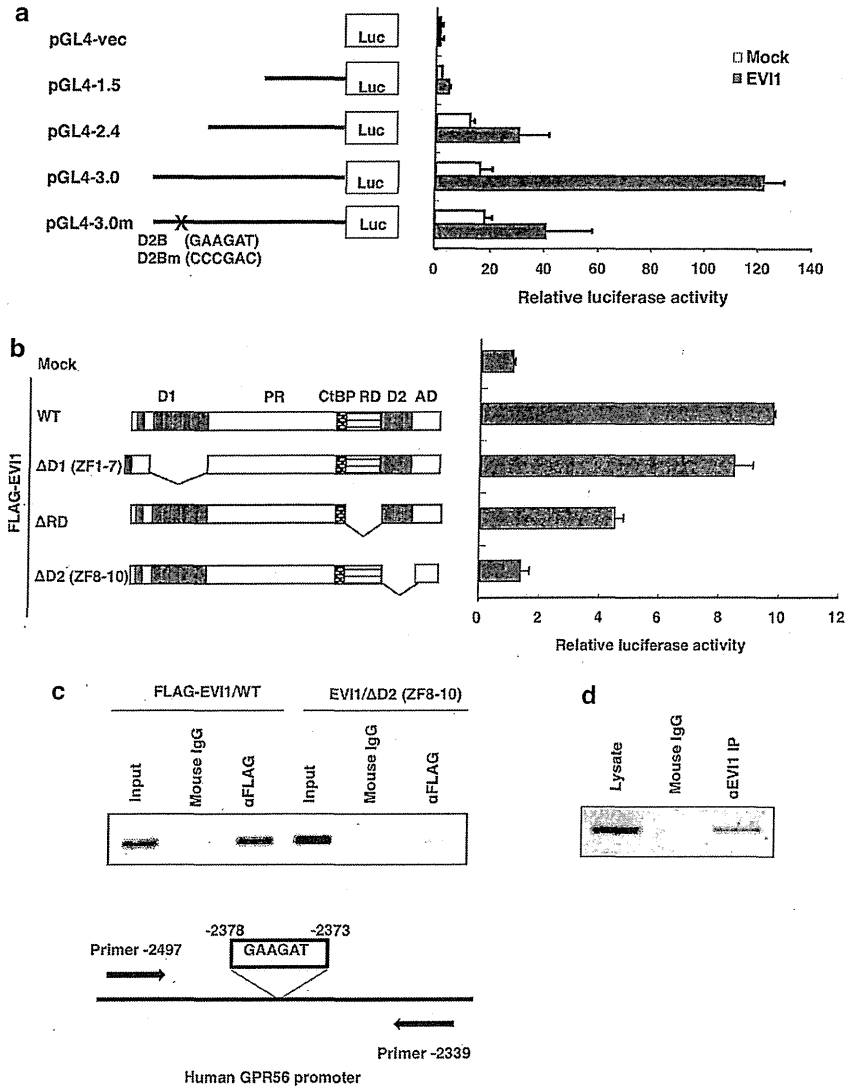

Figure 2. EVI1 binds to the promoter region of GPR56 to enhance its expression. (**a**) Structures of the GPR56 promoter region reporter plasmids are shown. A 1.5, 2.4 or 4.0 kb fragment of the GPR56 promoter region or a 4.0 kb fragment, in which GAAGAT was replaced with CCCGAC in the second ZF domain-binding sequence between −4.0 to −2.4 kb, was inserted upstream of the luciferase gene in the reporter plasmid pGL4. A mock reporter plasmid (pGL4-Vec) was used as a control. The fold change in promoter activity is shown as the ratio of normalized luciferase activity to the activity following control pGL4-Vec transfection. The open columns display the promoter activities of the various reporter plasmids, and the closed columns display the activities of a reporter plasmid in the presence of an EVI1 expression vector. All luciferase reporter assays were performed in duplicate in two independent experiments. The values and error bars depict the means ± s.d. (**b**) The structures of wild-type EVI1 and the EVI1 mutants with a series of deleted domains are depicted. COS7 cells were co-transfected with the GPR56 reporter vector, and each expression vector was co-transfected with EVI1 or EVI1 mutants (ΔD1 (ZF1-7), ΔRD, or ΔD2 (ZF8-10)). The fold change was calculated by dividing the fold activation of each EVI1 mutant co-transfected with pGL4-3.0 by the fold activation of the respective EVI1 mutant co-transfected with pGL4-vec. All of the luciferase reporter assays were performed in duplicate in two independent experiments. The values and error bars depict the means ± s.d. (**c**) Chromatin immunoprecipitation analysis of the EVI1-binding site in the GPR56 promoter region after transfection with the EVI1 expression vector is shown. After co-transfection with FLAG-tagged EVI1/WT or EVI1/ΔD2 (ZF8-10) with pGL4-3.0, formalin-fixed DNA fragments were immunoprecipitated with an anti-FLAG antibody or control mouse immunoglobulin G. The precipitated DNA was then amplified using specific primers to detect the EVI1-binding sites. (**d**) Chromatin immunoprecipitation of the endogenous EVI1 protein from UCSD/AML1 cells is shown. Formalin-fixed DNA fragments were immunoprecipitated with an anti-EVI1 antibody or control mouse immunoglobulin G. The precipitated DNA was then amplified using specific primers to detect the EVI1-binding sites.

cells with high or low GPR56 expression. After introduction of GPR56-specific small hairpin RNA or control small hairpin RNA into UCSD/AML1 cells, the expression of GPR56 was significantly decreased in UCSD/AML1/shGPR56 cells compared with the UCSD/AML1/shCNTL cell line (Figures 3a and b). The cellular adhesion of these lines was evaluated using either a feeder layer consisting of a murine osteoblastic cell line, MC3T3-E1, or using plates coated with fibronectin, Matrigel, laminin-1 or collagen type III. The adhesion of UCSD/AML1/shGPR56 cells to MC3T3-E1 cells and the various types of extracellular matrix was significantly impaired compared with that of the parental and UCSD/AML1/shCNTL cells (Figure 3c). Similar results were obtained for PT9 cells

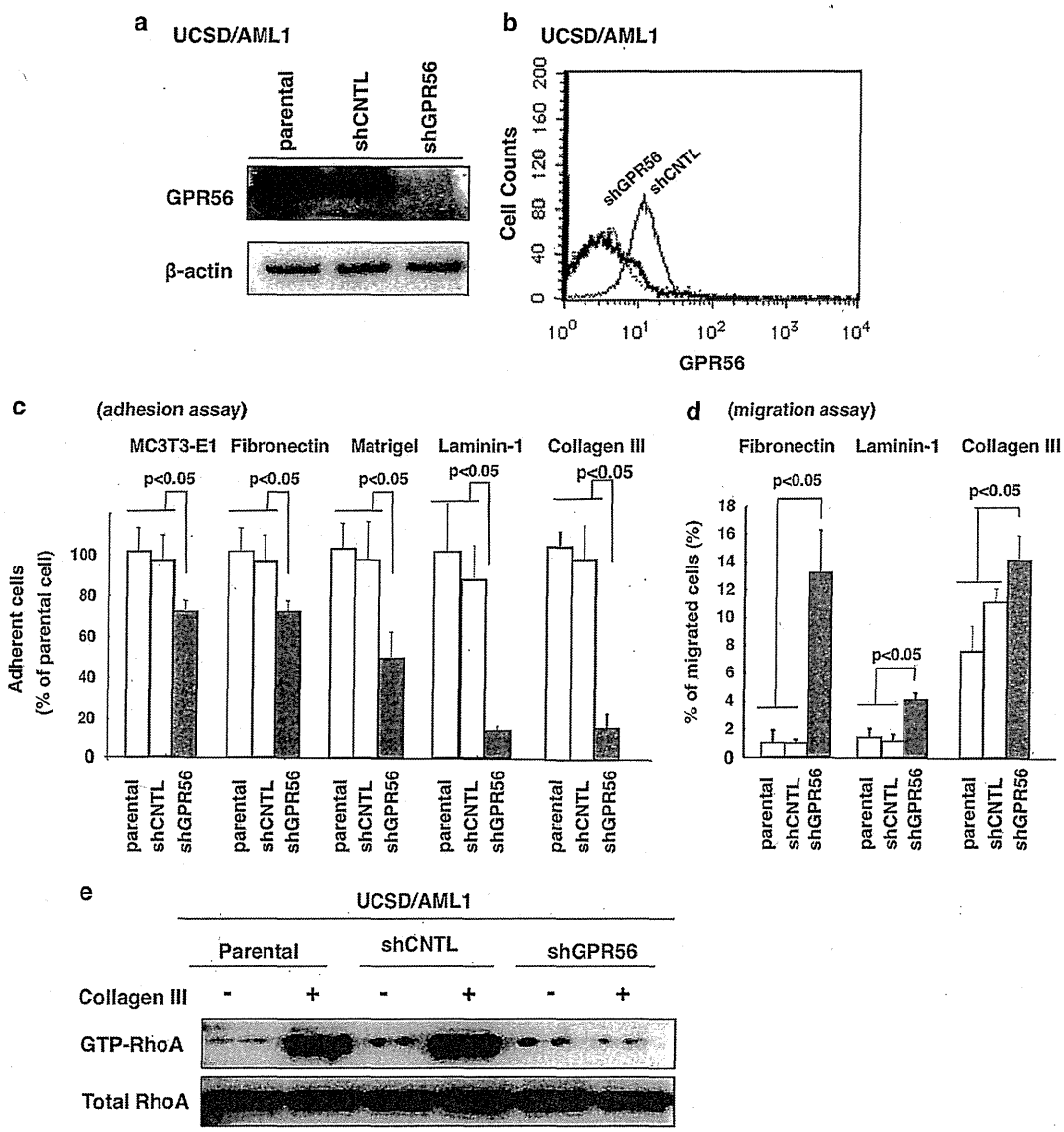

Figure 3. Knockdown of GPR56 expression increases the cell migration ability and decreases cellular adhesion to the extracellular matrix (ECM) through activation of the RhoA pathway. (**a**) Introduction of the shGPR56 expression vector into UCSD/AML1 cells downregulated GPR56 protein expression. The expression of GPR56 in parental UCSD/AML1, UCSD/AML1/shCNTL and UCSD/AML1/shGPR56 cells was detected with an anti-GPR56 antibody. (**b**) The cell surface expression of GPR56 in UCSD/AML1/shCNTL and UCSD/AML1/shGPR56 cells was determined by flow cytometric analysis. (**c**) The adhesion of parental UCSD/AML1, UCSD/AML1/shCNTL and UCSD/AML1/shGPR56 cells to MC3T3-E1 or ECM (fibronectin, Matrigel, laminin-1 or collagen type III) was quantified. The data are presented as the means ± s.d of the relative fold changes compared with the adherent cells in parental UCSD/AML1 cells. (**d**) The migration activities of the parental UCSD/AML1, UCSD/AML1/shCNTL and UCSD/AML1/shGPR56 cells through an ECM layer of fibronectin, laminin-1 or collagen type III were measured in response to an stromal cell-derived factor-1 (SDF-1α) gradient. The percentages of migrated cells are shown compared with the total cell numbers in this experiment. The data are presented as the means ± s.d. (**e**) The activated form of RhoA in parental UCSD/AML1, UCSD/AML1/shCNTL and UCSD/AML1/shGPR56 cells was measured via western blot analysis. The level of total RhoA in the cell lysates served as an internal control.

transfected with shGPR56 (PT9/shGPR56) (Supplementary Figures 3a and b). By contrast, the adhesion of U937/GPR56 cells was significantly increased compared with that of the parental and U937/Mock cells (Supplementary Figures 3c and d). To determine the cell migration abilities of the leukemia cells, the cells were added to the upper well of a Boyden chamber after fibronectin, laminin-1 or collagen type III had been embedded at the interface, and culture medium containing stromal cell-derived factor-1 was added to the bottom chamber. The number of migrating UCSD/AML1/shGPR56 cells was significantly increased compared with that of the parental and UCSD/AML1/shCNTL cells in the three different types of coated chambers (Figure 3d). Because the expression of CXCR4 was not significantly different between both cell types (Supplementary Figure 4), the increased migration ability mainly depended on the adhesion ability of the cells to the extracellular matrix in a Boyden chamber.

Collagen type III and other extracellular matrix molecules induce activation of the small GTP-binding protein RhoA downstream of GPR56;[31] therefore, we next determined the protein levels of GTP-bound RhoA in these cell lines. The level of GTP-bound RhoA in

parental and UCSD/AML1/shCNTL cells was increased after stimulation by collagen type III. However, the GTP-bound RhoA content in nonstimulated AML/shGPR56 cells was lower than the content in control cell lines, and stimulation with collagen type III did not increase the amount of GTP-bound RhoA in AML/shGPR56 cells (Figure 3e). To confirm whether activation of RhoA is necessary for the cellular adhesion of AML cells showing high GPR56 expression, Y-27632, a selective inhibitor of the Rho-associated protein kinase p160ROCK, was added to the culture medium of UCSD/AML1 cells. In control medium, UCSD/AML1 cells attached to conventional culture plates with a spindle-shaped cell morphology. However, the morphology of UCSD/AML1 cells changed from dendritic to small and round after the treatment with Y-27632 (Supplementary Figure 5a). In addition, the adhesion of UCSD/AML1 cells to MC3T3-E1 cells or to fibronectin was significantly decreased by treatment with Y-27632 (Supplementary Figure 5b). Therefore, the high level of cellular adhesion of EVI1^{high} AML cells was partially dependent on the expression of GPR56, and downstream RhoA activation has an important role in regulating cellular adhesion and cell migration in EVI1^{high} AML cells.

Involvement of GPR56 expression in apoptosis of EVI1^{high} AML cells

In the next set of experiments, we determined whether the expression of GPR56 affects the growth and viability of EVI1^{high} AML cells. After infection of recombinant shGPR56- or shCNTL-containing lentivirus into EVI1^{high} UCSD/AML1 and EVI1^{high} HNT34 cells, greater than 90% of the infected cells were GFP positive. Cell growth was determined immediately after infection. The growth rates of both cell lines transduced with shGPR56 (UCSD/AML1/shGPR56 and HNT34/shGPR56) were significantly decreased 3–5 days after infection compared with the growth rates of parental and shCNTL-infected cells (Figures 4a and b). Moreover, after introduction of the shGPR56 expression vector into PT9 cells, the colony-forming ability of parental PT9, PT9/shCNTL and PT9/shGPR56 cells was determined in methylcellulose cultures with GM- colony-stimulating factor. The colony number and size of granulocyte/macrophage colony-forming units were significantly reduced in PT9/shGPR56 cells (Supplementary Figures 6a and b). Therefore, we next determined whether apoptotic cell death was induced in shGPR56 cells. In a cell cycle analysis, an increase in the SubG1-phase cell population was observed in the UCSD/AML1/shGPR56 cells (Figure 4c). To confirm the induction of apoptotic cell death by GPR56 knockdown, lentivirus-infected cells were analyzed via flow cytometry after double staining with 7-Aminoactinomycin D and phycoerythrin-conjugated Annexin V (Figures 4d and e). The population of apoptotic cell death in the UCSD/AML1/shGPR56 cells was significantly increased compared with that in the UCSD/AML1/shCNTL cells several days after lentiviral infection, suggesting that the apoptosis of the UCSD/AML1/shGPR56 cells was due to the reduction of GPR56 expression. To determine the molecular mechanism underlying the inhibition of the apoptosis pathway downstream of GPR56 signaling, we determined the protein expression status of known apoptotic indicators and cell cycle regulators, including p53 and caspase-3 (Figure 4f). Cleaved caspase-3 fragments were detected in UCSD/AML1/shGPR56 cells, indicating that the apoptotic pathway was activated. Interestingly, the protein levels of p53, p21 and p27 were increased in UCSD/AML1/shGPR56 cells, whereas the level of MDM2 was proportionally decreased. However, the mRNA levels of p53 and MDM2 were unchanged in UCSD/AML1/shGPR56 cells compared with control UCSD/AML1 cells (Supplementary Figure 7), suggesting that an unknown signaling pathway downstream of GPR56 may stabilize the level of the MDM2 protein in EVI1^{high} AML cells, which promotes cell survival by promoting p53 degradation.

GPR56 expression was related to cell adhesion mediated drug resistance and the invasion ability of leukemic cells in BM

We next examined the role of GPR56 expression in the drug sensitivity of the cells to anticancer drugs. The UCSD/AML1 cells were seeded on MC3T3-E1 or BSA with various concentrations of Ara-C or daunorubicin (DNR) in culture media. Twenty-four hours after incubation, the percentages of surviving UCSD/AML1/shGPR56 cells on MC3T3-E1 cells (adherent status) were significantly reduced compared to the control UCSD/AML1 cells; however, the percentages of the UCSD/AML1/shGPR56 cells that survived under conventional culture condition were not different between the cells (Figures 5a and b). To determine the role of *GPR56 expression in drug resistance in vivo*, we performed xenotransplantation experiments of leukemia cells with high or low GPR56 expression into non-obese diabetic-severe combined immunodeficiency/γcnull (NOD-SCID/γcnull, NOG) mice. Initially, we determined the percentages of invaded leukemia cells in various organs two weeks after transplantation. Leukemia cells with high GPR56 expression (K562/GPR56 and UCSD/AML1) had a tendency to infiltrate into the BM more than other organs; however, leukemia cells with low GPR56 expression (K562/Mock and UCSD/AML1/shGPR56) infiltrated to the PB and other organs more than the BM (Figures 5c and d). To find the different effects of anticancer drugs on leukemia cells with high or low expression of GPR56 *in vivo*, mice transplanted with UCSD/AML1/shCNTL or UCSD/AML1/shGPR56 leukemia cells were treated with Ara-C for two weeks; at this time, the number of viable leukemia cells was determined in various organs by flow cytometry. The result showed that the USCD/AML1/shGPR56 cells were more effectively eliminated in the PB and spleen than in the BM (Figure 5e). Although we did not determine the survival curve of xenotransplanted mice undergoing anticancer treatment, the reduction of GPR56 expression in leukemia cells may help to enhance the sensitivity to anticancer drugs; further studies are needed to examine these effects.

High GPR56 expression in murine hematopoietic stem cell fractions and decreased numbers of HSCs in the BM of *Gpr56*$^{-/-}$ mice

Because GPR56, regulated by EVI1, is speculated to have an important function in the maintenance of HSCs, we next examined the expression of GPR56 in myeloid lineage cells at various stages of differentiation via flow cytometry analysis. Over 90% of LSK ($Lin^-Sca\text{-}1^+c\text{-}Kit^+$) cells expressed GPR56 on their cell surfaces, and more primitive self-renewing HSCs, including long-term and short-term HSCs, showed expression rates greater than 95% (Supplementary Table 3 and Supplementary Figure 8a). The level of GPR56 expression gradually decreased during the myeloid differentiation stages, and less than 50% of Lin^+ progenitor cells exhibited detectable GPR56 expression. In the BM in the diaphysis of tubular bones, high numbers of GPR56-positive cells were detected by fluorescence staining close to the periosteal rim, which is a region that contains potential BM osteosteal niches. The GPR56-positive mononuclear cells frequently coexpressed c-Kit and Sca-1, suggesting that $GPR56^+c\text{-}Kit^+$ primitive cells may localize near the periosteal region (Figure 6a and Supplementary Figure 8b). To determine the role of GPR56 in the regulation of hematopoiesis, we initially confirmed the downregulation of GPR56 expression in Lin^- BM cells in *Gpr56*$^{-/-}$ mice (Supplementary Figure 9a), and determined the hematological profiles in their PB. There were no differences in the blood cell counts or hemoglobin content between the wild-type and *Gpr56*$^{-/-}$ mice (Supplementary Table 4). There were also no differences in whole-BM cells and spleen cells (Supplementary Figure 9b). Interestingly, the percentages of LSK cells in the BM were significantly decreased, but the percentages in the spleen and the PB were conversely increased in the *Gpr56*$^{-/-}$ mice

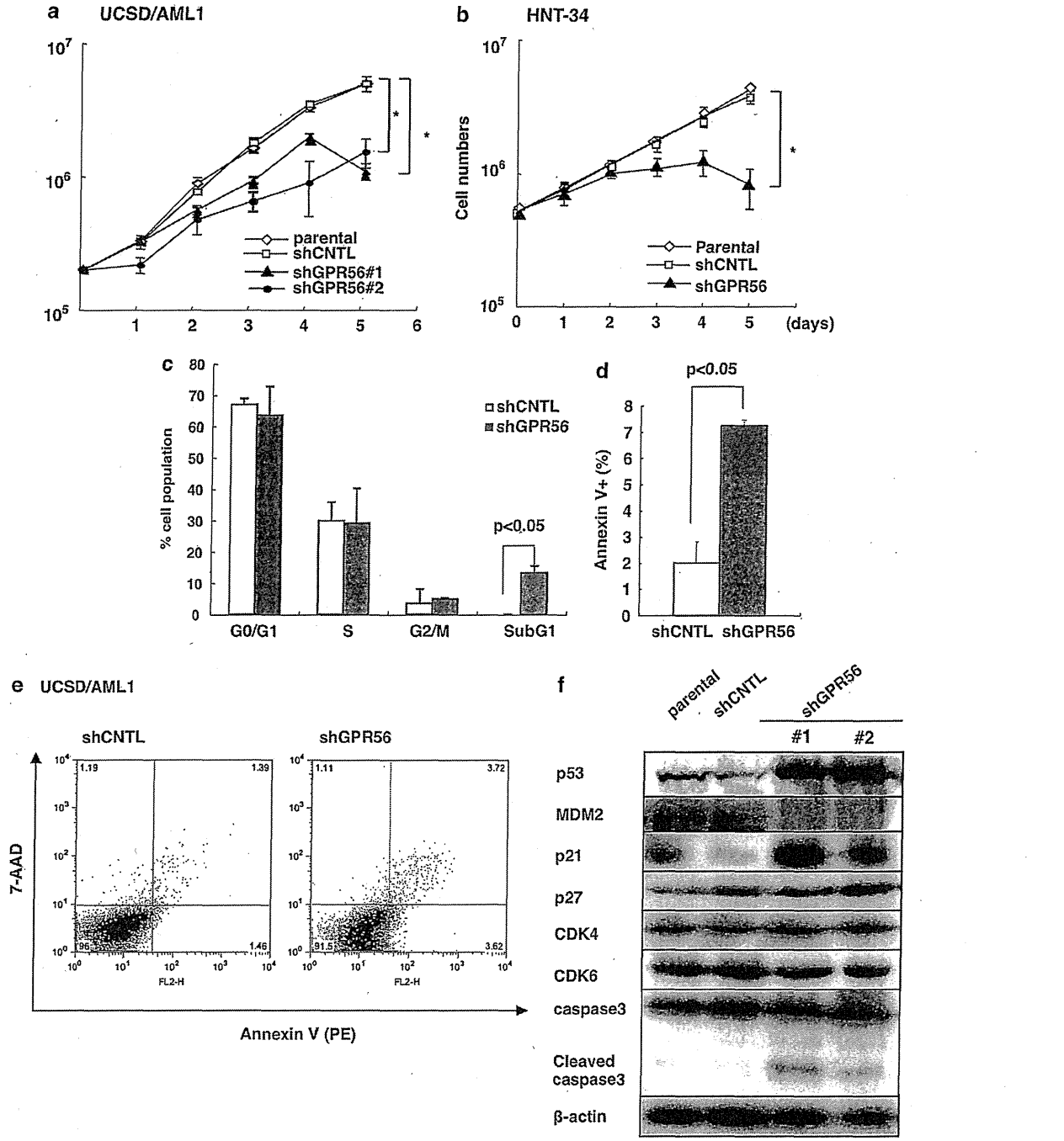

Figure 4. Knockdown of GPR56 expression induced apoptosis in EVI1^{high} leukemia cells through the accumulation of p53. (**a** and **b**) The influence of GPR56 knockdown on cell proliferation is shown. The growth rates of parental UCSD/AML1, UCSD/AML1/shCNTL and UCSD/AML1/shGPR56 cells and parental HNT34, HNT34/shCNTL and HNT34/shGPR56 cells were evaluated with the trypan blue exclusion assay. The live cells were counted after trypan blue staining using light microscopy. The data are presented as the means ± s.d. (**c**) Cell cycle fractions were analyzed by fluorescence-activated cell sorting after propidium iodide staining. The data are presented as the means ± s.d. (**d** and **e**). Six days after cell culture, UCSD/AML1/shCNTL and UCSD/AML1/shGPR56 cells were labeled with Annexin V and 7-aminoactinomycin D (7-AAD) and analyzed by flow cytometry. The percentages of Annexin V-stained dead cells are displayed as a bar graph (**d**), and the biparametric histogram represents the apoptotic cells, which show high Annexin V and low 7-AAD signals, and the secondary necrotic cells, which show high Annexin V and high 7-AAD signals (**e**). The experiments were performed in triplicate and repeated independently at least three times. (**f**) The expression of a series of apoptosis-related proteins was analyzed in various types of UCSD/AML1 cells by western blotting. Knockdown of GPR56 induced the accumulation of p53 by reducing the level of MDM2.

(Figures 6b and c). Moreover, the populations of short-term HSCs and long-term-HSCs were significantly reduced among the BM cells of the *Gpr56*$^{-/-}$ mice (Figure 6d). In the next experiment, we determined the colony-forming ability of mononuclear cells from the BM, spleen, liver and PB using semi-solid culture with several specific cytokines (Figure 6e). The number of granulocyte/

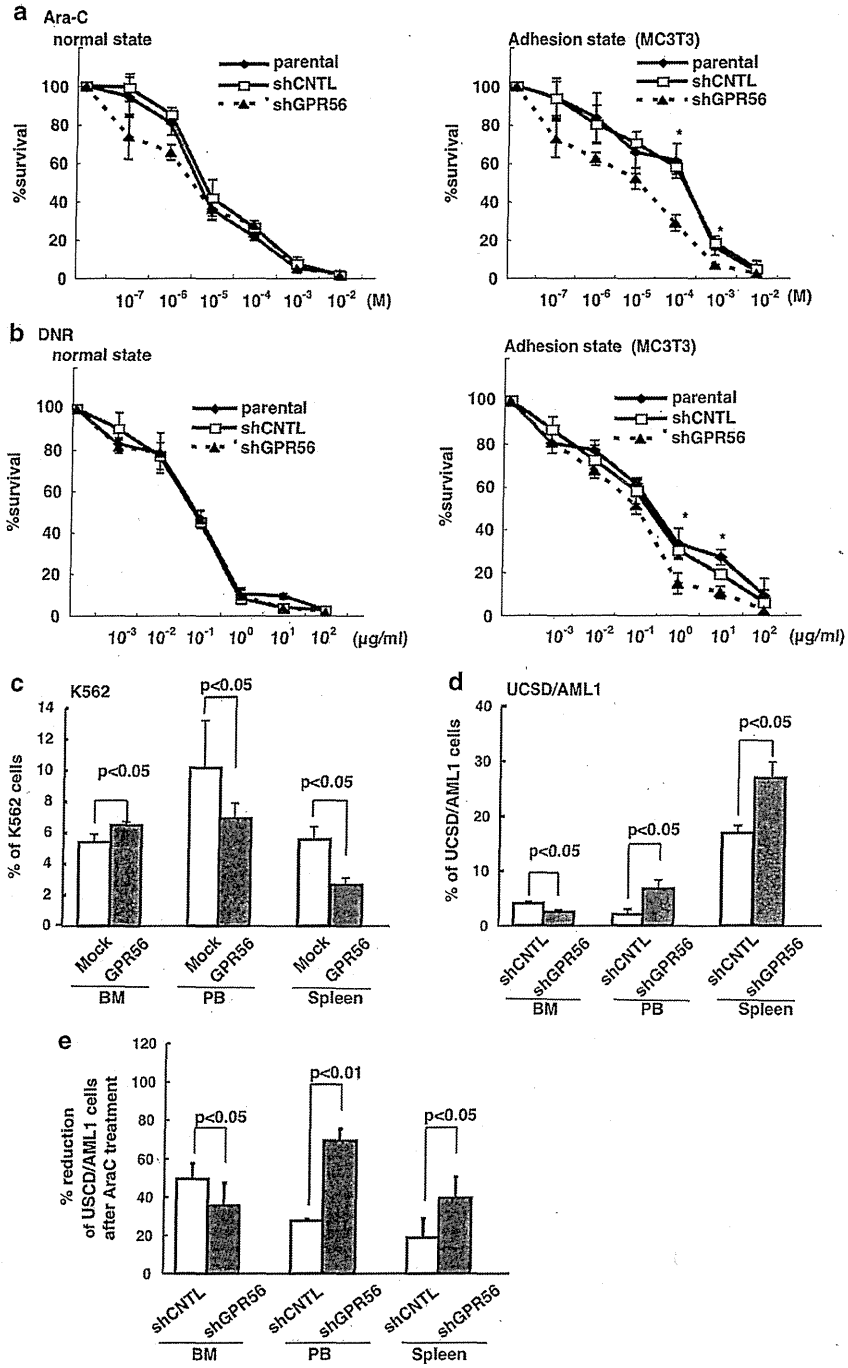

Figure 5. Knockdown of GPR56 inhibits drug resistance in AML cells, and GPR56 is an important regulator of leukemic cell engraftment. (**a** and **b**) The effect of adhesion on the chemosensitivity of UCSD/AML1, UCSD/AML1/shCNTL and UCSD/AML/shGPR56 cells is shown. UCSD/AML1 cells were incubated with Ara-C (**a**) or DNR (**b**) on MC3T3 coated plates. The number of viable cells and percentage of viable cells were assessed by trypan blue exclusion. The data are presented as the means ± s.d. Asterisks denote $P<0.05$ by Student's *t*-test. (**c**) K562/Mock cells or K562/GPR56 cells were intravenously transplanted into non-obese diabetic-severe combined immunodeficiency/γcnull (NOD-SCID/γcnull, NOG) mice. Two weeks after transplantation, the mice were killed, and the percentage of migration was analyzed. The means ± s.e. ($N=5$ per group), as evaluated by Student's *t*-test, are shown. (**d**) UCSD/AML1/shCNTL cells or UCSD/AML1/shGPR56 cells were intravenously transplanted into NOG mice. Two weeks after transplantation, the mice were killed, and the percentage of migration was analyzed. The means ± s.e. ($N=5$ per group), as evaluated by Student's *t*-test, are shown. (**e**) Mice were treated with Ara-C intravenously once per week (150 mg/kg). Two weeks after being treated with Ara-C, the mice were killed, and the percentage of the reduction in the leukemia cells was analyzed.

macrophage colony-forming units was significantly decreased in the BM of *Gpr56*$^{-/-}$ mice. However, granulocyte/macrophage colony-forming units and granulocyte, erythrocyte, monocyte/macrophage, megakaryocyte colony-forming unit (CFU-GEMM) numbers were clearly increased in the spleen, liver and PB of *Gpr56*$^{-/-}$ mice. Because the total colony numbers of

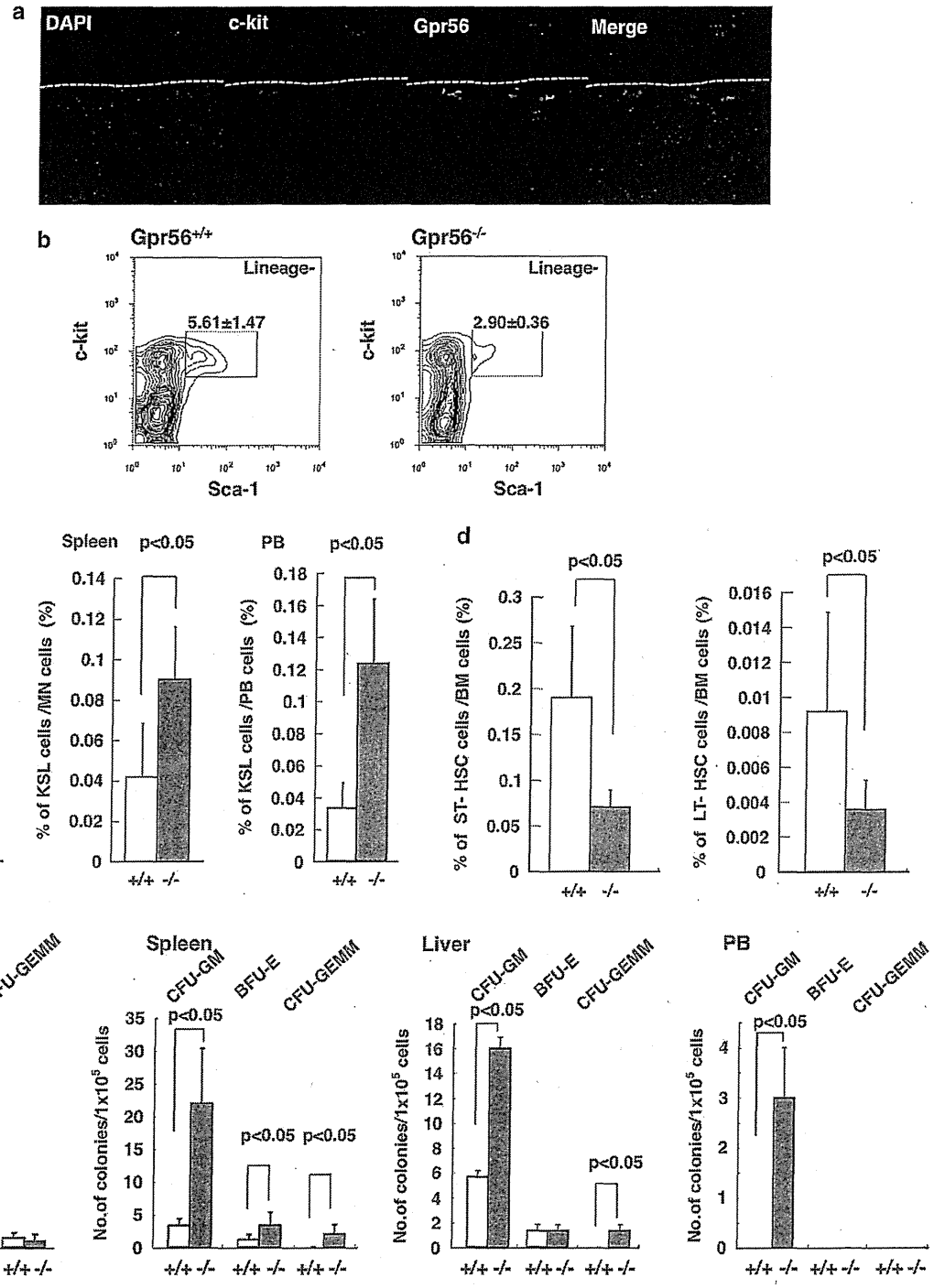

Figure 6. Decreased populations of HSCs in the BM of *Gpr56*$^{-/-}$ mice. (**a**) BM sections from wild-type mice were stained with 4′,6-diamidino-2-phenylindole (blue), c-Kit (red) and Gpr56 (white). c-Kit^{+}Gpr56^{+} cells resided near the periosteal region in the BM. (**b**) Populations of LSK cells were detected by flow cytometry and were isolated from the BM of 8-to 12-week-old wild-type (*Gpr56*$^{+/+}$) and *Gpr56*$^{-/-}$ mice (*Gpr56*$^{-/-}$). Data are presented as the mean percentages ± s.d. of LSK cells ($n=5$). (**c**) The percentages of LSK cells per total mononuclear cell (MNC) counts in the BM from two legs (left side), the spleen (middle) and the PB (right side) are shown as white bars (+/+) and gray bars (−/−). The proportion of LSK cells in the BM of *Gpr56*$^{-/-}$ mice was significantly decreased, whereas those proportions in the spleen and PB were significantly increased. The data shown are the mean percentages of LSK cells ($n=5$). (**d**) The population of short-term (left side) and long-term (LT) HSCs (right side) are shown as white bars (+/+) and gray bars (−/−). (**e**) The colony-forming abilities of MNCs from the BM, PB, spleens and livers of *Gpr56*$^{+/+}$ (+/+, white bar) and *Gpr56*$^{-/-}$ (−/−, gray bar) mice were determined in methylcellulose cultures by measuring granulocytes/monocytes colony-forming units(CFU-GM), erythroids (burst-forming unit-erythroid, BFU-E) and granulocytes/erythroids/monocytes/megakaryocytes (CFU-GEMM). The data shown are the mean numbers of colonies ($n=3$).

granulocyte/macrophage colony-forming units were maintained in Gpr56$^{-/-}$ mice, the numbers of white blood cells were most likely not decreased in Gpr56$^{-/-}$ mice. Therefore, a part of the HSCs in *Gpr56*$^{-/-}$ mice do not remain in the BM and relocate to the peripheral organs where they maintain their differentiation capacity.

Decreased cellular adhesion and increased cellular migration ability in HSCs from *Gpr56*$^{-/-}$ mice

To investigate whether the decreased number of HSCs in the BM is related to a reduction in their adhesion and acquisition of migration ability, we assessed cellular adhesion and the cell migration ability using BM precursor cells with the Lin$^-$c-Kit$^+$

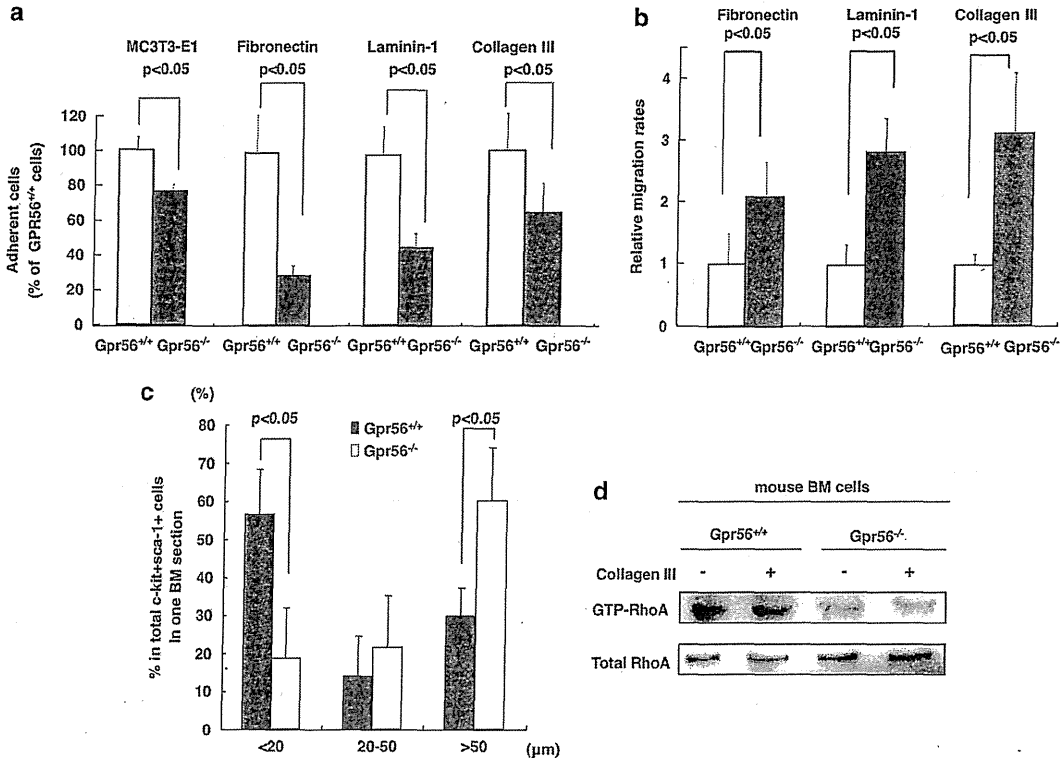

Figure 7. Increased migration and decreased cellular adhesion to the ECM of hematopoietic stem/progenitor cells from *Gpr56*$^{-/-}$ mice is induced through the RhoA pathway. (**a**) The adhesion of BM Lin$^-$c-Kit$^+$ (KL) cells from *Gpr56*$^{+/+}$ or *Gpr56*$^{-/-}$ mice to MC3T3-E1 adherent cells and three different types of ECM (fibronectin, laminin-1 or collagen type III) was measured, and the results are displayed as white bars (*Gpr56*$^{+/+}$) or gray bars (*Gpr56*$^{-/-}$). The strength of cellular adhesion is shown relative to the strength of KL cells from *Gpr56*$^{+/+}$ mice. The data are presented as the means ± s.d. ($n=3$) (**b**) The cellular migration of BM KL cells from wild-type or *Gpr56*$^{-/-}$ mice in response to an SDF-1α gradient is shown. Three different types of ECM interfaces (fibronectin, laminin-1 or collagen type III) were used in a Boyden chamber system in this experiment. The data are presented as the relative migration rates compared with the migration rates of KL cells from *Gpr56*$^{+/+}$ mice. The data are presented as the means ± s.d. ($n=3$) (**c**) The *in situ* localization of c-Kit$^+$ and Sca-1$^+$ cells within the femur BM of *Gpr56*$^{+/+}$ or *Gpr56*$^{-/-}$ mice was detected by immunohistochemistry. The localization of c-Kit$^+$ and Sca-1$^+$ cells was categorized into three groups based on the distance from the periosteum (<20, 20–50 and >50 μm). The data are presented as the means ± s.d. ($n=3$). (**d**) The protein level of GTP-bound RhoA in Lin$^-$c-Kit$^+$ BM cells from *Gpr56*$^{+/+}$ or *Gpr56*$^{-/-}$ mice was measured by western blot analysis. The protein level of total RhoA in the cell lysates served as a control.

Figure 8. The expression of GPR56 in HSCs is involved in the maintenance of quiescence and LT BM reconstitution. (**a**) After collecting LSK cells labeled with Annexin V-PE and 7-AAD, the populations (%) of early apoptotic cells were counted using Annexin V$^+$ and 7-AAD$^-$ staining, and are displayed as white bars (*Gpr56*$^{+/+}$) or dark bars (*Gpr56*$^{-/-}$). The data are presented as the means ± s.d. ($n=3$). (**b**) Following bromodeoxyuridine (BrdU) incorporation *in vivo*, LSK cells from *Gpr56*$^{+/+}$ (white bar) and *Gpr56*$^{-/-}$ (gray bar) mice were isolated and stained with an allophycocyanin (APC)-conjugated anti-BrdU antibody and 7-AAD to analyze the cell cycle stage by flow cytometry. The data are presented as the means ± s.d. ($n=3$). (**c**) After staining LSK cells from *Gpr56*$^{+/+}$ (left) and *Gpr56*$^{-/-}$ mice (right) with Hoechst 33342 and pyronin Y, the populations (%) of LSK cells in the G0-phase of the cell cycle were assessed via flow cytometry. The data are presented as the means ± s.d. ($n=3$). (**d**) *Gpr56*$^{+/+}$ and *Gpr56*$^{-/-}$ mice were administered 5-fluorouracil intraperitoneally once per week for 2 weeks, and the survival of individual mice was monitored daily. The results were analyzed using a log-rank nonparametric test, and the survival rates of *Gpr56*$^{+/+}$ (solid line) and *Gpr56*$^{-/-}$ (dotted line) mice were plotted on a Kaplan–Meier curve ($n=6$). (**e**) For competitive repopulation assays, donor BM cells or LSK cells from CD45.2$^+$ *Gpr56*$^{+/+}$ or *Gpr56*$^{-/-}$ mice were mixed in a 1:1 or 1:50 ratio with CD45.1$^+$ competitor cells and transplanted into lethally irradiated CD45.1$^+$-recipient mice. (**f** and **g**) The chimerism in the first transplantation was measured as the number of white blood cells from the PB (**f**) and as the number of lineage-negative c-Kit-positive cells from the BM (Lin$^-$c-Kit$^+$ BM) (**g**). (**h** and **i**) The chimerism in the second transplantation was measured as the number of white blood cells from the PB (**h**) and as the number of lineage-negative cells from the BM (Lin$^-$c-Kit$^+$ BM) (**i**) The data shown are the mean percentages ± s.d. of donor-derived cells in the PB at 4 weeks after transplantation ($n=5$). The chimerism in Lin$^-$c-Kit$^+$ BM cells was determined by flow cytometry 16 weeks post-transplantation ($n=5$). (**j** and **k**) LSK cells from CD45.2$^+$ wild-type or *Gpr56*$^{-/-}$ mice were used for a competitive repopulation assay. The chimerism in the transplantation was measured as the number of white blood cells from the PB (**j**) and as the number of lineage-negative c-Kit-positive cells from the BM (Lin$^-$c-Kit$^+$ BM) (**k**). The data shown are the mean percentages ± s.d. of donor-derived cells in the PB at 4 weeks after transplantation ($n=4$).